IVYSPRING INTERNATIONAL PUBLISHER

Theranostics

2027; 17(1): 468-487. doi: 10.7150/thno.135541

Research Paper

α7nAChR-dependent macrophage-to-fibroblast signaling ameliorates atrial remodeling by inhibiting fibroblast ANKRD1-mediated fibrosis

Ling Dong[1,2,3], Yiwen Wang[1,4], Zhenduo Zhang[1,3], Jiyuan Zhan[1,3], Liming Yu[1], Tao Huang[1], Ting Yan[5], Tong Su[1,4], Yinli Xu[1], Zijun Zhou[1], Boxuan Sun[1], Liman Yang[5], Jikai Zhao[1]✉, Jinsong Han[1]✉, Huishan Wang[1]✉

1. State Key Laboratory of Frigid Zone Cardiovascular Disease, Department of Cardiovascular Surgery, General Hospital of Northern Theater Command, No. 83 Wenhua Road, Shenyang 110016, Liaoning, China.
2. Department of Cardiovascular Ultrasound, The First Hospital of China Medical University, No. 155 Nanjing North Street, Shenyang, Liaoning, China.
3. The First Affiliated Hospital of Dalian Medical University, No. 222 Zhongshan Road, Dalian 116011, Liaoning, China.
4. College of Medicine and Biological Information Engineering, Northeastern University, No. 11 Wenhua Road, Shenyang 110819, Liaoning, China.
5. Department of Pathology, General Hospital of Northern Theater Command, No. 83 Wenhua Road, Shenyang, Liaoning 110016, China.

✉ Corresponding authors: Jikai Zhao, M.D., State Key Laboratory of Frigid Zone Cardiovascular Disease, Department of Cardiovascular Surgery, General Hospital of Northern Theater Command, 83 Wenhua Road, Shenyang City 110016, China. E-mail: zhaojk1002@hotmail.com. Jinsong Han, M.D., State Key Laboratory of Frigid Zone Cardiovascular Disease, Department of Cardiovascular Surgery, General Hospital of Northern Theater Command, 83 Wenhua Road, Shenyang City 110016, China. E-mail: hanjs0216@sina.com. Huishan Wang, M.D., State Key Laboratory of Frigid Zone Cardiovascular Disease, Department of Cardiovascular Surgery, General Hospital of Northern Theater Command, 83 Wenhua Road, Shenyang City 110016, China. Tel: +86 24 28897382, E-mail: huishanw@126.com.

© 2027 The Author(s). This is an open access article distributed under the Creative Commons Attribution 4.0 International Licence, subject to the Publisher's Terms of Use at https://ivyspring.com/terms.

Received: 2026.04.02; Accepted: 2026.09.27; Published: 2027.01.01

Abstract

Rationale: Atrial fibrillation (AF) is the most prevalent clinical manifestation of cardiac arrhythmias, and its pathogenesis is driven by macrophage-mediated inflammation and fibrosis, both of which are associated with the α7 nicotinic acetylcholine receptor (α7nAChR). However, the role and mechanism of α7nAChR in macrophage-fibroblast crosstalk during AF pathogenesis have not been elucidated. This work aims to examine the function of macrophage α7nAChR-mediated macrophage-to-fibroblast fibrotic signaling in atrial fibrillation.

Methods and Results: We established an angiotensin II (Ang II)-elicited AF mouse model, in which α7nAChR activity was modulated either by intraperitoneal administration of the selective agonist GTS-21 or by genetic deletion of α7nAChR (Chrna7-KO). GTS-21 treatment markedly reduced the susceptibility to AF elicited by Ang II and attenuated the remodeling of atrial electrical and structural properties, whereas α7nAChR deficiency exacerbated these effects. Macrophage α7nAChR was identified as a pivotal regulator of atrial fibrosis, mediating IL-10 related M2c polarization both *in vivo* and *in vitro*. Bulk RNA sequencing revealed that α7nAChR activation modulated Ankyrin repeat domain 1 (ANKRD1)-associated fibrotic signaling. Mechanistically, a Transwell system was employed to establish a co-culture model of macrophages and fibroblasts. Western blotting, co-IP, and ChIP assays demonstrated that macrophage α7nAChR inhibited fibroblast ANKRD1 nuclear translocation and its interaction with AP-1 (c-Fos/c-Jun), thus reducing MMP9 transcription and fibrotic activation. *In vivo*, macrophage-specific α7nAChR overexpression significantly alleviated Ang II-induced atrial fibrosis and remodeling, which were abolished by fibroblast-specific ANKRD1 overexpression.

Conclusions: Our findings elucidate a critical mechanism integration linking macrophage α7nAChR activity with fibroblast ANKRD1 signaling to mediate fibrosis in Ang II-induced atrial remodeling. The macrophage α7nAChR-IL-10-fibroblast ANKRD1 axis represents a potential therapeutic target that requires further validation in additional disease models and human tissues.

Keywords: atrial fibrillation, macrophage, α7nAChR, ANKRD1, fibrosis

Introduction

Atrial fibrillation (AF), as the predominant prevalent form of persistent cardiac arrhythmia, carries significant morbidity and mortality rates, placing significant strains on both healthcare systems and economic development [1]. Approximately 33.5 million individuals were affected by AF in 2010, with projections suggesting a threefold increase over the next three decades [2]. AF induces cardiac remodeling

characterized by structural and electrical alterations [3]. Previous studies have emphasized that significant immune system alterations occur during AF, especially in hypertension-associated inflammatory atrial fibrillation, involving dynamic interactions with the microenvironment and cells responsible for initiating and sustaining AF [4, 5]. In addition, fibrotic remodeling features of AF serve as both consequences and active drivers of immune remodeling, thus creating a self-reinforcing cycle that perpetuates AF. Moreover, fibroblasts promote atrial fibrosis through excessive extracellular matrix (ECM) deposition, which contributes to atrial fibrillation refractoriness and ectopic pacing point generation [6, 7]. However, the specific biological mechanisms that drive hypertension-driven inflammatory AF progression have yet to be completely elucidated.

During the fibrotic remodeling of AF, macrophages release inflammatory cytokines and engage in cross-talk with other cell types. Functionally, macrophages polarize into two major phenotypes: the pro-inflammatory M1 phenotype and the anti-inflammatory, tissue-repair M2 phenotype [8]. Additionally, studies have shown that high serum levels of M1 macrophage inflammatory markers are corelated with left atrial fibrosis and enlargement in AF, characterized by fibroblast activation and collagen deposition [9, 10]. However, increasing evidence indicates that M2 macrophages, which have traditionally been regarded as a single subtype, are heterogeneous. In contrast to the pro-fibrotic role of M1 macrophages, this population primarily promotes repair processes in the tissue microenvironment and can be further subdivided into M2a, M2b, and M2c subtypes. Specifically, M2a macrophages participate in both tissue repair and fibrosis via MMT, whereas M2c macrophages exhibit strong anti-inflammatory properties and facilitate tissue repair through IGF-1 secretion [11, 12]. Nevertheless, the role of macrophages in regulating fibroblasts and the underlying mechanism mediating atrial fibrosis have not been fully elucidated.

α7nAChR (α7 nicotinic acetylcholine receptor) serves as a pentameric ligand-gated ion channel that plays multiple signaling roles in physiological functions [13]. Notably, macrophages are the primary immune cell type expressing α7nAChR [14]. As a ligand-gated ion channel, α7nAChR is highly permeable to Ca^{2+} and promotes Ca^{2+} influx, resulting in positive biological effects [15]. Furthermore, it has been shown that α7nAChR ameliorates myocardial fibrosis and cardiac function by inhibiting inflammatory responses in disease models such as heart failure and viral myocarditis [16, 17]. α7nAChR activation decreases pro-inflammatory cytokine release and produces anti-inflammatory effects mediated through reduced M1 polarization and promotion of phenotypic switching [18]. Specifically, α7nAChR activation promotes the generation of $CD163^+$ M2c macrophages and upregulates anti-inflammatory cytokine IL-10 levels, thus modulating the balance between M1 and M2c polarization to exert anti-inflammatory effects [19]. Based on this, it has been suggested that α7nAChR has a positive effect on improving cardiac function [20]. Therefore, macrophage α7nAChR activation and expression could be promising candidates for attenuating fibrosis in hypertension-driven inflammatory AF, but the underlying mechanism needs further clarification.

Ankyrin repeat domain 1 (ANKRD1) is a member of the conserved muscle anchor in the repeat protein family, and plays a critical role in pathological cardiac remodeling [21]. ANKRD1 demonstrates dual subcellular localization, functioning as a transcription factor in the nucleus while interacting with myosin in the cytoplasm to maintain sarcomeric organization [22]. With respect to cardiovascular pathology, upregulation of ANKRD1 expression and functional activation in fibroblasts have been demonstrated in mouse models of dilated cardiomyopathy and angiotensin II (Ang II)-triggered cardiac fibrosis [23, 24]. Specifically, nuclear translocation of ANKRD1 in cardiac fibroblasts is closely associated with matrix metalloproteinase (MMP)-mediated collagen synthesis and extracellular matrix deposition [25]. However, ANKRD1 is also responsive to inflammatory mediators [26, 27], suggesting its potential involvement in macrophage-fibroblast crosstalk during AF progression. Therefore, the precise mechanism underlying the relationship between macrophage α7nAChR signaling and fibroblast ANKRD1 activation remains undefined.

Here, we demonstrated in Ang II-elicited AF mice that macrophage α7nAChR prevents fibrosis and atrial remodeling by restoring M2c macrophage polarization. Mechanistically, macrophage α7nAChR modulates the progression of fibrosis by releasing IL-10 to inhibit ANKRD1 nuclear translocation and suppress AP-1/MMP9 signaling in fibroblasts.

Materials and Methods

Animals and treatment

Male C57BL/6J wild-type (WT) mice, 10 weeks of age, were obtained from HUAFUKANG (Beijing, China). Housing conditions included an SPF environment, with temperature kept at 22 ± 2 °C, a 12-h light-dark cycle, and food and water supplied without restriction. To minimize environmental stress, a one-week acclimatization period was given to all

mice before any experimental intervention. Approval for all animal procedures was granted by the Animal Care Committee of General Hospital of Northern Theater Command (Ethical Number: 8210013). Our study used a previously described method for AF modeling in mice [28]. Briefly, mice were administered Ang II at 1800 ng/kg/min (A9525, Sigma-Aldrich, USA) for 28 days via subcutaneous infusion using an osmotic pump (Alzet Model 2004; Durect, California, USA). To examine the role of activating α7nAChR on AF, mice received treatment with the α7nAChR agonist GTS-21 (HY-14564A, MedChemExpress, USA) or with 0.9% saline via intraperitoneal injection (2 mg/kg/day) combined with/without 4-weeks Ang II infusion. To explore the role of decreased α7nAChR in AF, we obtained 10-week-old male Chrna7 knockout (Chrna7-KO) mice from Cyagen Biotechnology (Suzhou, China) and kept them under the same feeding conditions as WT mice, which would be treated by Ang II or vehicle for a 4-week period. To validate the involvement of macrophage α7nAChR in mediating fibroblast ANKRD1 expression in AF, we constructed an adeno-associated virus (AAV) 9 vector with an F4/80 promoter containing the Chrna7 sequence (AAV-F4/80-Chrna7^{oe}) for macrophage-specific α7nAChR gene overexpression and with a TCF21 promoter containing the ANKRD1 sequence (AAV-TCF21-ANKRD1^{oe}) for fibroblast-specific ANKRD1 gene overexpression (Hanbio, Shanghai, China). Eight-week-old male WT mice were treated with AAV-F4/80-Chrna7^{oe} and/or AAV-TCF21-ANKRD1^{oe} (2×10^{12} vg/mL, 100 μL) by tail vein injection. Two weeks after viral injection, the mice were subjected to a 4-week Ang II infusion for AF modeling. Weekly monitoring and weighing were performed on all the mice throughout the study. At the end of the 4-week Ang II-induced AF model, the animals were euthanized, and their atria were excised for further experimentation.

Echocardiography in mice

Following a 4-week infusion of Ang II, anesthesia was induced in the mice with 2% isoflurane. An ultrasonic imaging device with high-resolution Doppler capability (D700, Vinno Technology, China) was used for cardiac function assessment, with a modified version of a previously described protocol [29]. We acquired echocardiographic images in the parasternal left ventricular long-axis view for no fewer than three sequential heartbeats, and used M-mode echocardiography to measure the left ventricular ejection fraction (LVEF), left atrial systolic area (LAAs), left atrial diastolic area (LAAd), left atrial diameter (LAD). Data analysis was conducted using the manufacturer's proprietary software.

ECG recording and transjugular atrial electrical stimulation

We administered 1% sodium pentobarbital to induce anesthesia in mice, which were then placed supine on a surgical platform. Continuous electrocardiographic (ECG) recordings were obtained using a three-lead ECG monitoring system (FE132-0641, ADInstruments, China) and analyzed with LabChart 8 software [29]. The right jugular vein was surgically exposed, and an electrode catheter (EPR-800, ADInstruments, China) was advanced into the right atrium. Atrial burst pacing was performed using electrical stimuli set to 5 V, 40-ms cycle intervals, and 6-ms pulse widths, over a 30-s period. Successful AF induction was established when AF episodes occurred following at least two of every three pacing attempts. We defined AF as an atrial rhythm that was irregular and rapid, with a duration of >2 s, and measured its duration from the onset of arrhythmia to the spontaneous restoration of sinus rhythm.

Atrial electrophysiological mapping

We injected sodium pentobarbital (150-200 mg/kg) intraperitoneally to anesthetize and euthanize the mice. The thoracic cavity was opened to expose the heart below the xiphoid process. Oxygenated Tyrode's solution (37 °C, 15 mL/min, pH 7.0) was perfused through the Langendorff system after the heart had been rapidly excised and placed on it, which is consistent with previously described methods [30]. After stabilization, a 64-channel multi-electrode array (MappingLab Ltd., UK) used for conduction signal recording was positioned perpendicularly on the left atrial surface. EMap Record 5.0 software was used to analyze the conduction parameters, including the absolute inhomogeneity, the inhomogeneity index, and the average conduction velocity.

Masson's trichrome staining

After euthanasia, we rapidly excised the hearts. The atrial tissues were carefully separated and immediately rinsed in phosphate-buffered saline (PBS). We then submerged the tissues in 4% paraformaldehyde (C104190, Aladdin, China) for fixation, embedded them in paraffin and sliced them into 5-μm sections. For histological assessment, we stained the sections with a Masson's trichrome stain kit (C0189S, Beyotime Biotechnology, China) in accordance with the kit protocols [31]. The fibrotic area percentage was measured using ImageJ (NIH, USA).

Bulk RNA sequencing

We employed the Hieff NGS® MaxUp™ II Dual-mode mRNA Library Prep Kit for Illumina® to construct libraries for bulk RNA sequencing. Reads

were then mapped and quantified against reference genes using featureCounts (Subread v2.0.3). All differential expression analyses were performed in RStudio (2023.06.0 Build 421) with the limma package, applying criteria of $|\log_2 \text{fold change}| > 1$ and $p < 0.05$ to define differentially expressed genes (DEGs). Heatmaps were generated using TBtools-II [32]. For functional annotation, we uploaded the DEG lists to DAVID (v3.5.20240101) for enrichment of Kyoto Encyclopedia of Genes and Genomes (KEGG) and Gene Ontology (GO) pathways, while gene set enrichment analysis (GSEA) was performed with GSEA software (v4.3.2; Broad Institute/UC San Diego). Overlaps among DEGs across all group comparisons were identified and visualized with UpSet diagrams generated via the R package UpSetR [33].

Immune infiltration analysis

ImmuCellAI-mouse was used to evaluate the immune infiltration (https://guolab.wchscu.cn/ImmuCellAI-mouse/#!/) [34]. The infiltration of 36 immune cell types was separately evaluated using ImmuCellAI-mouse based on the differentially expressed genes (DEGs) identified from comparisons of Ang II versus Control and Ang II + GTS-21 versus Ang II. The resulting datasets were analyzed via intergroup differential analysis using the Wilcoxon test, and the outcomes were visualized with ggplot2.

Cell preparation and treatment

The Raw264.7 cells (mouse macrophages) used in the study were acquired from the American Type Culture Collection (TIB-71, ATCC, USA), and NCTC clone 929 (L929) cells (mouse fibroblasts) and mouse primary cardiac fibroblasts (mPCFs) were purchased from iCell Bioscience Inc (iCell-m026 and MIC-iCell-c002 Shanghai, China). Cells were grown in DMEM (G4520, Servicebio, China) supplemented with 10% FBS (G8003-100ML, Servicebio, China) and 1% penicillin-streptomycin (G4003-100ML, Servicebio, China) at 37 °C under a humidified 5% CO_2 atmosphere. BMDMs were isolated from mouse femurs and tibias. These cells were then differentiated in DMEM containing 10% FBS and M-CSF for 5 days. Mature BMDMs were then harvested for subsequent experiments. We treated the cells with 10 μmol/L Ang II (A9525; Sigma-Aldrich, USA) dissolved in DMSO, while the controlgroup was given 0.1% (v/v) DMSO only. GTS-21 (10 μmol/L, HY-14564A, MCE, USA) was used to activate macrophage α7nAChR *in vitro*. To investigate the mediating effect of IL-10, L929 cells and mPCFs were treated by recombinant mouse IL-10 (50 ng/mL, HY-P70517, MCE, USA) [35]. The α7nAChR overexpression (Chrna7^{oe}) plasmid, the ANKRD1 overexpression (Flag-ANKRD1^{oe}) and knockdown (siANKRD1) plasmids, and the IL10ra knockdown (siIL10ra) plasmid, along with their corresponding negative controls, were obtained from Sangon Biotech (Shanghai, China). Cells were transfected with LipoFiter 3.0 (HB-LF3-1000, Hanbio, China) following the manufacturer's protocol. We used a Transwell co-culture system to investigate the mechanism of macrophage-fibroblast crosstalk. In the Transwell co-culture system, Raw264.7 cells or BMDMs were cultured in the upper chamber and L929 cells or mPCFs were cultured in the lower chamber. Cells were exposed to Ang II and transfected with plasmids according to the groups.

Cell viability assay

A Cell Counting Kit-8 (CCK-8, KGA317s, KeyGEN Biotech, China) was used to measure cell viability. 96-well plates were seeded with Raw264.7 cells and BMDMs at 5,000 cells per well (100 μL), and we added 10 μL of the reagent after treatment. After a 2-h incubation at 37 °C in 5% CO_2, we used a microplate reader to record the absorbance at 450 nm (SPECTROstar Omega, BMG LABTECH, Germany).

Immunofluorescence staining

We subsequently fixed frozen sections (4 μm) or cultured cells in 4% paraformaldehyde for 10 min, treated them with 0.2% Triton X-100 (A417820, Sangon Biotech, China) for 10 min to permeabilize them, and then blocked them with 10% bovine serum albumin (BSA) (A8020, Solarbio, China) for 1 h. The following primary antibodies were used for overnight incubation at 4 °C: iNOS (sc-7271, Santa Cruz, 1:200), Arg1 (93668, CST, 1:200), CD68 (97778, CST, 1:500), α7nAChR (sc-58607, Santa Cruz, 1:300), F4/80 (ab300421, Abcam, 1:300), Ankrd1 (11427-1-AP, Proteintech, 1:300), α-SMA (67735-1-Ig, Proteintech, 1:400), and α-Actinin (ab1081980, Abcam, 1:300). After three washes with PBS, the samples were probed for 2 h at 37 °C with secondary antibodies: Alexa Fluor 488/568 donkey anti-mouse IgG (A32766 and A10037) and Alexa Fluor 488/568 donkey anti-rabbit IgG (A21206 and A10042), each from Invitrogen, at 1:300. After mounting samples with an anti-fading DAPI-containing medium (G1407-25ML, Servicebio, China), we acquired images with a Nikon C2 Plus confocal microscope and analyzed them using ImageJ.

Enzyme-linked immunosorbent assay (ELISA)

Levels of IL-10 (RK00016), IL-6 (RK00008), IL-1β (RM17859) and TNF-α (RK00027) were detected with ELISA kits (ABclonal, China) as directed by the manufacturer.

Flow cytometry

Primary atrial macrophages were isolated from mouse atria by enzymatic digestion using collagenase II and DNase I, followed by filtration and differential adhesion to remove cardiomyocytes, as previously described [4]. After three washes with sterile PBS, the Raw264.7 cells were gently detached from 6-well plates, centrifuged at 1000 rpm for 5 min, and then re-suspended in 100 µL of PBS after discarding the supernatant. Cells were incubated with antibodies against CD45.2 PE-CF549 (109846, BioLegend, 1:300) in primary atrial cells, CD206-APC (17-2061-82, eBioscience, 1:300), CD86-PE (12-0862-82, eBioscience, 1:300), CD163-PE-Cy7 (155319, BioLegend, 1:300), MERTK-FITC (2B10C42, BioLegend, 1:300), Zombie Violet Dye (77477, BioLegend, 1:300) for 30 min at 4 °C, rinsed with PBS, and analyzed using a BD FACSCelesta flow cytometer (BD Biosciences, USA). FlowJo software (v10.8.1, TreeStar, USA) was used to process the data.

Quantitative real-time PCR (qPCR)

Total RNA was isolated from cells using TRIzol (Invitrogen, USA), and cDNA was synthesized using a reverse transcription kit (Takara, Japan) following the supplier's instructions. Quantitative real-time PCR was performed on a QuantStudio 6 Flex System (Applied Biosystems, USA) in a 25-µL reaction mixture containing 12.5 µL of 2× SYBR Green Master Mix (Takara, Japan), 0.5 µL each of forward and reverse primers (10 µM), 2.5 µL of diluted cDNA, and 9 µL of RNase-free water. Relative expression was quantified using the $2^{-\Delta\Delta Ct}$ method and normalized to Gapdh; primer sequences are listed in Table S1.

Chromatin immunoprecipitation (ChIP) and ChIP-qPCR

Chromatin immunoprecipitation (ChIP) assays were carried out according to a published protocol with slight changes. L929 cells underwent crosslinking with 1% formaldehyde for 20 min at room temperature; the reaction was then quenched using 0.125 M glycine. After cell lysis in a buffer supplemented with protease inhibitors (Sigma-Aldrich, USA), the chromatin was fragmented into 200–500 bp fragments via sonication with a Bioruptor (Diagenode, Belgium). We collected 20 µL of the supernatant as input DNA after centrifugation at 4 °C for 10 min. Using protein A–agarose beads (Millipore, USA), the remaining chromatin was cleared at 4 °C for 3 h and subsequently incubated overnight with 5 µg of anti-c-Fos (2250, CST), anti-c-Jun (9165, CST), or normal rabbit IgG. Sequential washing of the beads was performed with low-salt, high-salt, LiCl, and TE buffers. After proteinase K treatment (Roche, USA) for 1 h at 37 °C to reverse crosslinking, the DNA was recovered by ethanol precipitation. The purified DNA was then quantified via qPCR using SYBR Green Master Mix (Takara, Japan). We calculated enrichment as a percentage of the input or as a fold change over the IgG control, using primers targeting the AP-1 site (chr2: 164,781,800–164,781,812, + strand) within the Mmp9 promoter (Forward: 5′-GCTGTTGGGGTAGGAACAGG-3′; Reverse: 5′-GCTGCTACAGGACATCAGGG-3′). On the next day, the beads were mixed with 40 µL of fresh protein A–agarose beads and incubated for another 2 h at 4 °C.

Co-immunoprecipitation (Co-IP) assay

Co-immunoprecipitation (Co-IP) assays were conducted to evaluate protein-protein interactions according to a published procedure with minor modifications. Ice-cold IP lysis buffer (MCE, USA) was added to cells, and the mixture was incubated on ice for 30 min.

After centrifugation at 12,000 × g for 10 min at 4 °C, cellular debris was pelleted, and the supernatants were collected. For each sample, 500–1000 µg of total protein was combined with 30 µL of anti-Flag magnetic beads (MCE, USA) and left to incubate overnight at 4 °C. After five washes with chilled lysis buffer, we boiled the beads in 2× SDS sample buffer for 5 min to elute the bound proteins. Eluates were subsequently separated via SDS-PAGE and transferred to membranes for immunoblotting with the designated antibodies. To serve as loading references, input aliquots (5–10% of the total lysate) were also loaded alongside them.

Western blot analysis

Atrial tissues or cells were incubated in RIPA buffer containing phosphatase inhibitors (1:100) and phenylmethylsulfonyl fluoride (1:100). Following BCA quantification, equal protein amounts from each group were separated by SDS-PAGE, transferred to PVDF membranes, and blocked with 5% BSA in PBS containing 0.1% Tween-20. Membranes were incubated with primary antibodies: α7nAChR (ab216485, Abcam, 1:600), IL-6 (sc-65327, Santa Cruz, 1:1000), IL-1β (A16288, ABclonal, 1:500), IL-10 (60269-1-Ig, Proteintech, 1:300), TNF-α (sc-52746, Santa Cruz, 1:600), CD163 (16646-1-Ig, Proteintech, 1:600), CD206 (18704-1-Ig, Proteintech, 1:500), Arg1 (93668, CST, 1:500), iNOS (727111, Santa Cruz, 1:300), COL1A1 (sc-293182, Santa Cruz, 1:800), COL3A1 (sc-514601, Santa Cruz, 1:800), MMP9 (sc-21733, Santa Cruz, 1:800), MMP2 (sc-13595, Santa Cruz, 1:800), α-SMA (A2235, ABclonal, 1:1000), Ankrd1 (11427-1-AP, Proteintech, 1:600), c-Jun (sc-74543, Santa Cruz, 1:600), c-Fos (74620,

CST, 1:500), β-actin (2D4H5, Proteintech, 1:1000), GAPDH (A19056, Abclonal, 1:100000), α-Tubulin (A6830, Abclonal, 1:1000) overnight at 4 °C and followed by 1 h incubation with secondary antibodies at 37 °C. Signals were subsequently acquired using a Tanon imaging system, and ImageJ software was used to quantify band intensities.

Statistical analysis

Data are expressed as means ± SDs. Intergroup differences between two groups were assessed by an unpaired Student's t-test; for multiple-group comparisons, one-way or two-way analysis of variance (ANOVA) followed by Tukey's post hoc test was used. Fisher's exact test was adopted to assess AF inducibility. A p-value < 0.05 was considered statistically significant. GraphPad Prism (version 9.5; GraphPad Software, USA) was used for all statistical analyses and data plotting.

Results

Activation of α7nAChR by GTS-21 alleviates Ang II-induced atrial electrical and structural remodeling

To investigate the role of α7nAChR in Ang II-treated atrial fibrillation in mice, we administered the α7nAChR-selective agonist GTS-21 or saline intraperitoneally for four weeks, with or without concurrent Ang II infusion (Figure 1A). The results demonstrated that α7nAChR expression of mice atria was significantly downregulated in the Ang II-treated group relative to the Control group, which was reversed by GTS-21 treatment (Figure 1B-C). AF susceptibility was evaluated by transjugular pacing. Following programmed electrical stimulation, both AF incidence and duration increased significantly in Ang II-treated mice relative to Controls. These changes were markedly mitigated in mice receiving combined Ang II and GTS-21 treatment (Figure 1D-F). High-resolution electrophysiological mapping of atria in Langendorff-perfused hearts showed that the absolute inhomogeneity index was elevated and mean conduction velocity was reduced by Ang II, and these effects were abolished by GTS-21 treatment (Figure 1G-I). Echocardiographic assessment further demonstrated that Ang II infusion resulted in a decline in left ventricular ejection fraction (LVEF) and atrial enlargement characterized by increased diameter (LAD), left atrial systolic area (LAAs) and diastolic area (LAAd), which were significantly alleviated by GTS-21 administration (Figure 1J-N). Collectively, these results indicate that activation of α7nAChR by GTS-21 mitigates Ang II-treated atrial electrical and structural remodeling, thus decreasing AF susceptibility.

Macrophage M2c polarization driven by α7nAChR activation is a critical regulator of the amelioration of Ang II-induced atrial remodeling

To further investigate the function of α7nAChR-mediated protection against AF, we conducted bulk RNA sequencing (RNA-seq) of Control, Ang II and Ang II + GTS-21 groups. GO pathway and GSEA analyses demonstrated that upregulated DEGs in the atria were predominantly enriched in inflammatory response pathways in the comparison between Ang II and Control (Figure 2A). In contrast, when the Ang II + GTS-21 group was compared with the Ang II group, downregulated DEGs showed significant enrichment in inflammatory response pathways using GO pathways and GSEA analyses (Figure 2B). Given the established role of α7nAChR in the macrophage-dependent cholinergic anti-inflammatory pathway (CAP) [36], we examined α7nAChR localization within atrial macrophages using immunofluorescence. The co-localization of the macrophage marker F4/80 with α7nAChR was reduced in the Ang II-treated group and enhanced by GTS-21 treatment (Figure 2C, Figure S1A), indicating macrophage-specific regulation of α7nAChR expression *in vivo*. ImmuCellAI-based immune infiltration analysis demonstrated that M1 macrophage abundance was elevated in the Ang II group and markedly decreased following GTS-21 treatment, whereas the abundance of M2 macrophages tended to decrease (Figure 2D). Moreover, the expression of the M1 marker iNOS was elevated in Ang II-treated atria but decreased in the Ang II + GTS-21 group, whereas the expression of the M2 marker Arg1 was upregulated in the Ang II + GTS-21 group (Figure S1B-D). Accordingly, Western blot quantification revealed that Ang II treatment markedly elevated proinflammatory cytokines (IL-6, IL-1β, and TNF-α) compared with Controls, which GTS-21 administration markedly reversed these changes (Figure S1E-F). Importantly, the expression of M2c markers (CD163 and CD206) significantly increased in the GTS-21 group, reversing the low expression induced by Ang II, which was accompanied by the secretion of IL-10 (an anti-inflammatory cytokine) (Figure 2E-F). Mouse atrial tissue was subsequently subjected to flow cytometric analysis (Figure S2A). Ang II infusion increased the M1/M2 ratio ($CD86^+CD206^-$/$CD86^-CD206^+$) of atrial macrophages and decreased the percentage of $CD163^+MERTK^+$ cells among $CD86^-CD206^+$ atrial macrophages, and these effects were reversed by GTS-21 (Figure 2G-J).

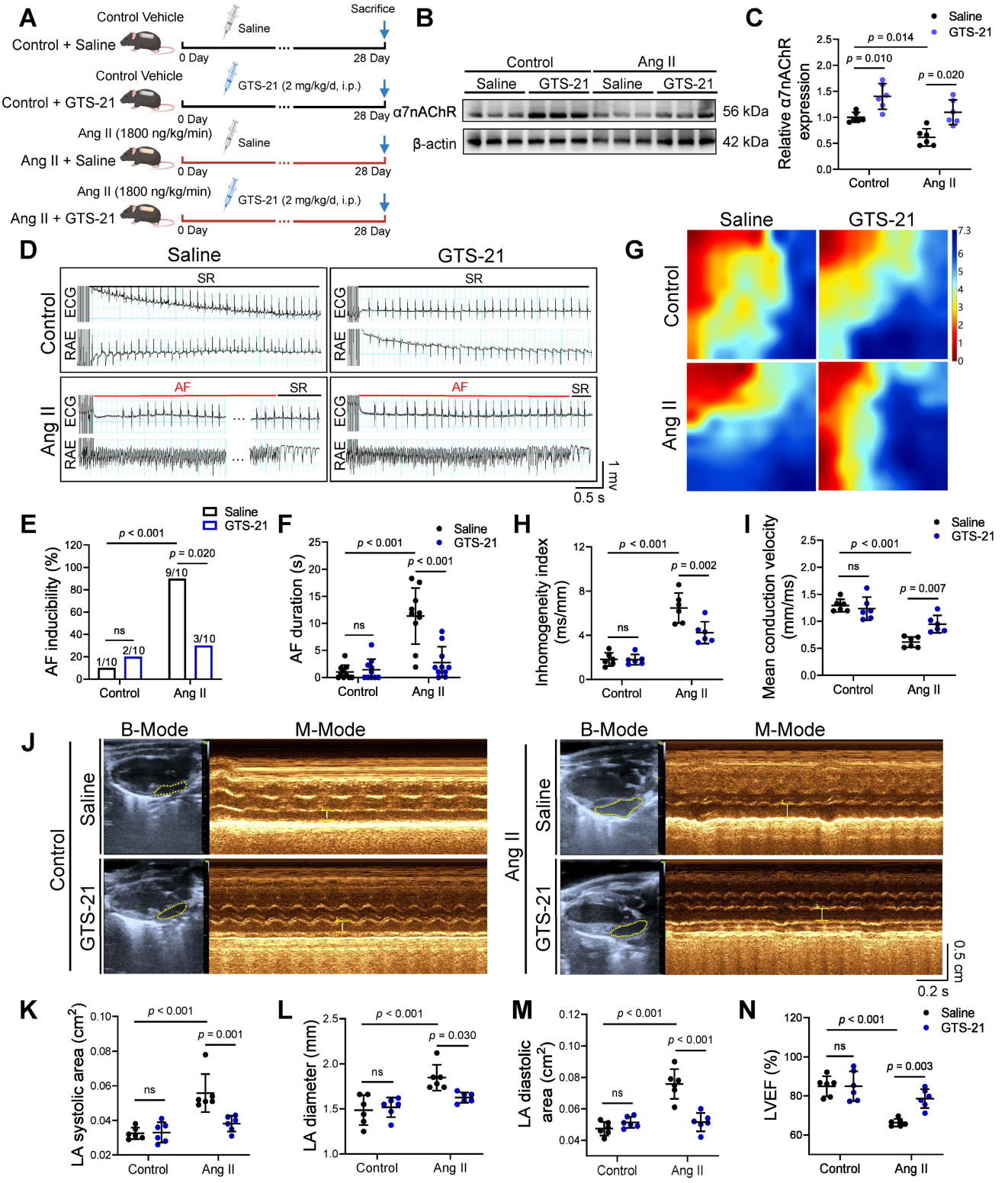


Figure 1. Activation of α7nAChR by GTS-21 alleviates Ang II-induced atrial electrical and structural remodeling. (A) An Ang II-induced AF model in mice was established with parallel Saline and GTS-21 treatment groups. (B-C) Western blots with quantification of relative α7nAChR expression *in vivo* (n = 6). (D) Representative electrograms from surface ECG and right atrium (RAE) obtained during and after atrial pacing. (E-F) Quantified were both AF inducibility and AF duration (n = 10). (G) Representative electrophysiological maps of left atria. (H-I) Left atrial conduction parameters were quantitatively evaluated by employing an electrophysiological mapping system (n = 6). (J) Representative images showing echocardiographic positioning and M-mode recordings (scale bar = 5 mm; time scale bar = 200 ms). (K-N) Left atrial diastolic area (LAAd), left atrial systolic area (LAAs), left atrial diameter (LAD), and left ventricular ejection fraction (LVEF) were quantified by M-mode echocardiography (n = 6). For statistics: two-way ANOVA with Tukey's post hoc test and Fisher's exact test (for AF inducibility) were used; error bars denote S.D.; $p < 0.05$ considered significant; ns, not significant.

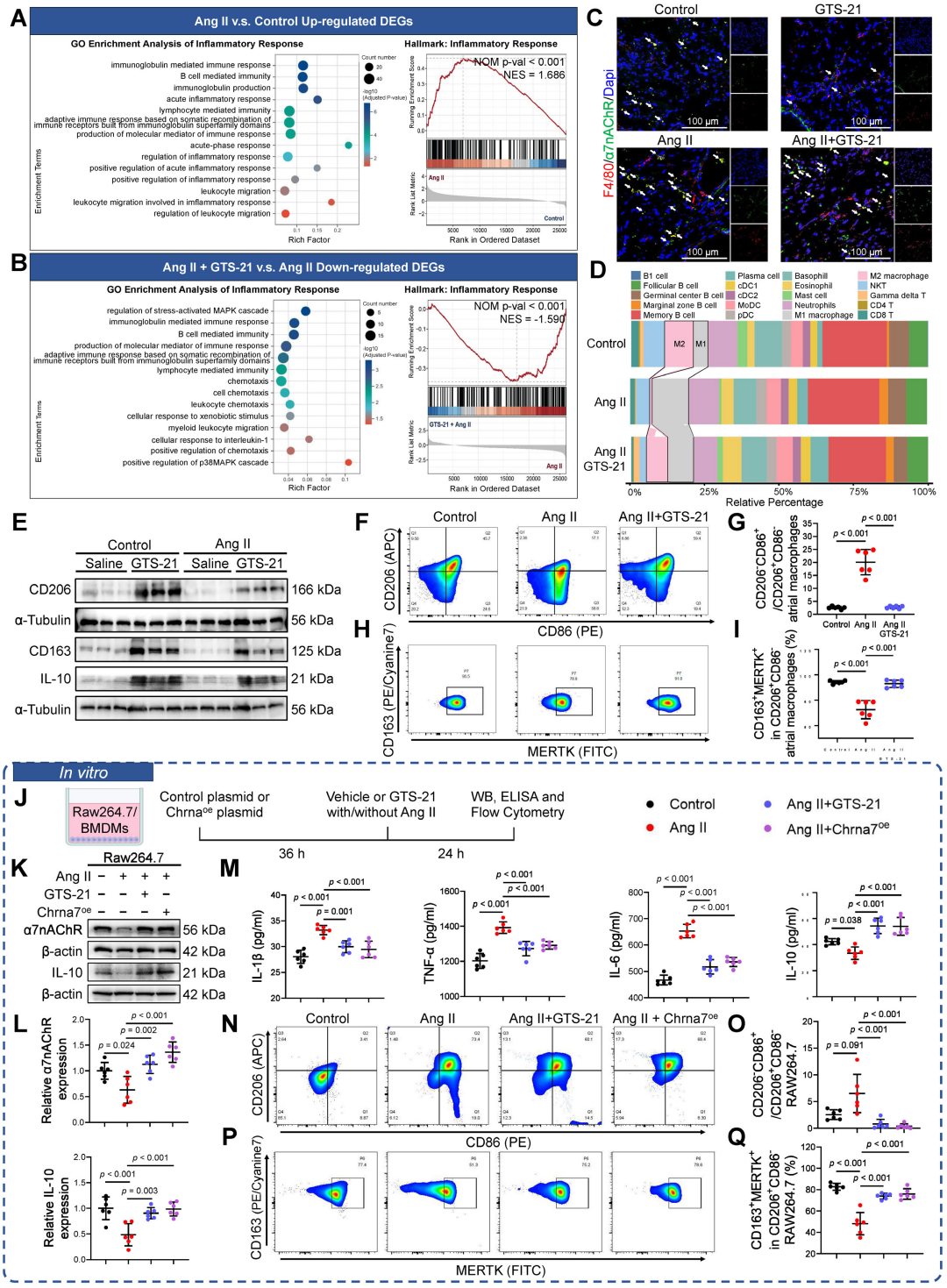


Figure 2. Macrophage M2c polarization driven by α7nAChR activation is a critical regulator in the amelioration of Ang II-induced atrial remodeling. (A-B) GO enrichment analyses of inflammatory of up-regulated DEGs of Ang II versus Control and down-regulated DEGs of Ang II + GTS-21 versus Ang II. Enrichment score is plotted on the horizontal axis, and the color gradient denotes adjusted p-value significance. (C) Representative immunofluorescence detection of F4/80 (red), α7nAChR (green), and DAPI (blue) in Control, GTS-21-treated, Ang II-infused, and Ang II + GTS-21-treated mice, with white arrows indicating co-localization of α7nAChR and F4/80 (scale bar = 100 μm). (D) Stacked bar chart of immune cell infiltration between Control, Ang II and Ang II + GTS-21 groups. (E) Representative Western blots for CD206, CD163, and IL-10 protein expression *in vivo* (n = 6). (F) Representative flow cytometry images of CD86 (M1 marker) and CD206 (M2 marker) atrial macrophages treated with Ang II and GTS-21. (G) Quantification of the M1 ($CD86^+CD206^-$) to M2 ($CD86^-CD206^+$) ratio (n = 6). (H) Representative flow cytometry images of CD163 (M2c marker), and MERTK (M2c marker) atrial macrophages treated with Ang II and GTS-21. (I) Quantification of the M2c ($CD163^+/MERTK^+$) percentage among $CD206^+/CD86^-$ atrial macrophages (n = 6). (J) Schematic diagram illustrating the treatment process of Raw264.7 macrophages and BMDMs. (K-L) Western blotting and quantification of relative α7nAChR and IL-10 expression in Raw264.7 macrophages incubated with/without Ang II, GTS-21, or Chrna7 overexpression ($Chrna7^{oe}$) (n = 6). (M) Quantification of IL-1β, TNF-α, IL-6 and IL-10 levels in conditioned medium of Raw264.7 macrophages exposed with/without Ang II, GTS-21, or $Chrna7^{oe}$ (n = 6). (N-Q) Representative flow cytometry images of CD86 (M1 marker), CD206 (M2 marker), CD163 (M2c marker), and MERTK (M2c marker) and quantitative analysis of the percentages of M1 ($CD86^+CD206^-$), M2 ($CD86^-CD206^+$), and M2c ($CD163^+/MERTK^+/CD206^+/CD86^-$) Raw264.7 macrophages treated with/without Ang II, GTS-21, or Chrna7 overexpression (n = 6). For statistics: one-way (G, I, L, M, O and Q) ANOVA with Tukey's post hoc test was used; error bars denote S.D.; $p < 0.05$ considered significant; ns, not significant.

To determine the effects of α7nAChR activation on macrophage polarization states, we generated a GTS-21 or *Chrna7*-specific (the coding gene of α7nAChR) overexpression plasmid (Chrna7^{oe}) in Ang II-treated Raw 264.7 cells and BMDMs (Figure 2K, Figure S3A-F). Both GTS-21 and Chrna7^{oe} reversed the downregulation of α7nAChR and IL-10 expression mediated by Ang II in Raw 264.7 cells and BMDMs (Figure 2L-M, Figure S4A-B). ELISA of the cell supernatant revealed that GTS-21 of Chrna7^{oe} suppressed the Ang II-induced elevation of pro-inflammatory cytokines (IL-1β, TNF-α, and IL-6) and reduction of anti-inflammatory cytokine (IL-10) in Raw 264.7 cells and BMDMs (Figure 2N, Figure S4C). Following Ang II treatment, BMDMs exhibited an M1-like round, pancake-shaped morphology; however, treatment with GTS-21 or Chrna7^{oe} induced a transition to an elongated spindle shape, which was consistent with the M2 phenotype (Figure S4D). Flow cytometric analysis of Raw264.7 macrophage polarization states (Figure S5A) revealed that the M1/M2 ratio ($CD86^+CD206^-/CD86^-CD206^+$) exhibited a significant elevation in Ang II-treated Raw264.7 cells versus controls, which was ameliorated by GTS-21 of Chrna7^{oe} (Figure 2O-P). We further subdivided the classification of M2 macrophages. Flow cytometry analyses showed a marked reduction in the abundance of $CD86^-CD206^+CD163^+MERTK^+$ macrophages, despite their upregulation following GTS-21 or Chrna7^{oe} treatment (Figure 2Q-R). In summary, these findings indicate that macrophage α7nAChR contributes to Ang II-induced atrial remodeling by promoting IL-10-related M2c macrophage polarization.

Inhibition of fibrotic signaling underlies the protective effect of macrophage α7nAChR activation on atrial remodeling mediated by IL-10

Subsequently, top GOBP and KEGG enrichment analyses of downregulated DEGs in the Ang II + GTS-21 versus Ang II comparison revealed significant involvement in extracellular matrix (ECM) organization, extracellular structure organization, collagen fibril organization, and the ECM–receptor interaction pathway (Figure 3A). GSEA confirmed that the DEGs were predominantly enriched in ECM-related signaling pathways (Figure 3B-C). Masson's trichrome staining revealed extensive atrial fibrosis in the Ang II group, and GTS-21 treatment markedly alleviated this fibrosis (Figure 3D-E). Consistent with these findings, GTS-21 significantly reduced the Ang II-induced upregulation of fibrotic markers (COL1A1, COL3A1 and α-SMA) and ECM-associated enzymes (MMP2 and MMP9) (Figure 3F-G). To examine the function of the M2c polarization marker IL-10 in the anti-fibrotic effects of macrophage α7nAChR, we constructed a Transwell co-culture system with Ang II in which Raw 264.7 macrophages or BMDMs in the upper chamber were treated with Chrna7^{oe} (mac-Chrna7^{oe}) to upregulate α7nAChR expression, while L929 fibroblasts or mPCFs in the lower chamber were transfected with siIL10ra (fib-siIL10ra) to downregulate IL-10 receptor level (Figure 3H). Western blot quantification revealed that Chrna7^{oe} in Raw 264.7 macrophages or BMDMs attenuated the expression of COL1A1, COL3A1, α-SMA, MMP2, and MMP9 in Ang II-treated L929 fibroblasts and mPCFs, and this ameliorative effect was inhibited by IL-10ra knockdown in the fibroblasts (Figure 3I-J, Figure S6A-B). These findings indicate that α7nAChR-activated M2c macrophage polarization mitigates Ang II-induced fibrosis, highlighting an α7nAChR related macrophage-fibroblasts axis in AF.

Loss of α7nAChR exacerbates Ang II-induced atrial remodeling in Chrna7-KO mice

To further delineate the role of α7nAChR in Ang II-induced atrial remodeling, α7nAChR knockout (Chrna7-KO, Figure S7A) mice were employed, with or without Ang II infusion for four weeks (Figure 4A). As expected, α7nAChR expression was notably lower in the atria of Ang II-induced Chrna7-KO mice than in those from Ang II-elicited WT mice (Figure S7B). AF susceptibility testing revealed higher AF incidence in both the Ang II (8/10) and Chrna7-KO (7/10), especially in the Ang II + Chrna7-KO group (10/10) relative to WT group (1/10). Moreover, AF duration was markedly prolonged in the Ang II + Chrna7-KO group compared with all other groups (Figure 4B-C). Langendorff perfusion mapping demonstrated reduced mean conduction velocity and elevated absolute inhomogeneity index in the Ang II, Chrna7-KO, and Ang II + Chrna7-KO groups relative to WT, with the most severe electrical impairment observed in the Ang II + Chrna7-KO group (Figure 4D-E). Consistent with these findings, echocardiographic evaluation demonstrated that LAAs, LAAd, and LAD were significantly greater in the Ang II, Chrna7-KO, and Ang II + Chrna7-KO groups compared with WT controls. Notably, atrial enlargement was most pronounced in the Ang II + Chrna7-KO group (Figure 4F-G). Compared with the Ang II group, Ang II-treated Chrna7-KO mice exhibited elevated TNF-α levels, without significant changes in IL-1β or IL-6, and a marked reduction in IL-10 expression (Figure 4H-I). In terms of fibrosis, Masson staining revealed more extensive collagen deposition in the Ang II + Chrna7-KO group than in either the Chrna7-KO or Ang II groups alone (Figure 4J-K). Consistently, the level of

fibrosis-related proteins, including α-SMA, COL1A1, COL3A1, MMP2, and particularly MMP9, were notably upregulated in Ang II + Chrna7-KO mice relative to Ang II mice (Figure 4L-M). Collectively, these results indicate that genetic deletion of α7nAChR exacerbates Ang II-treated atrial electrical and structural remodeling, thus promoting heightened AF vulnerability.

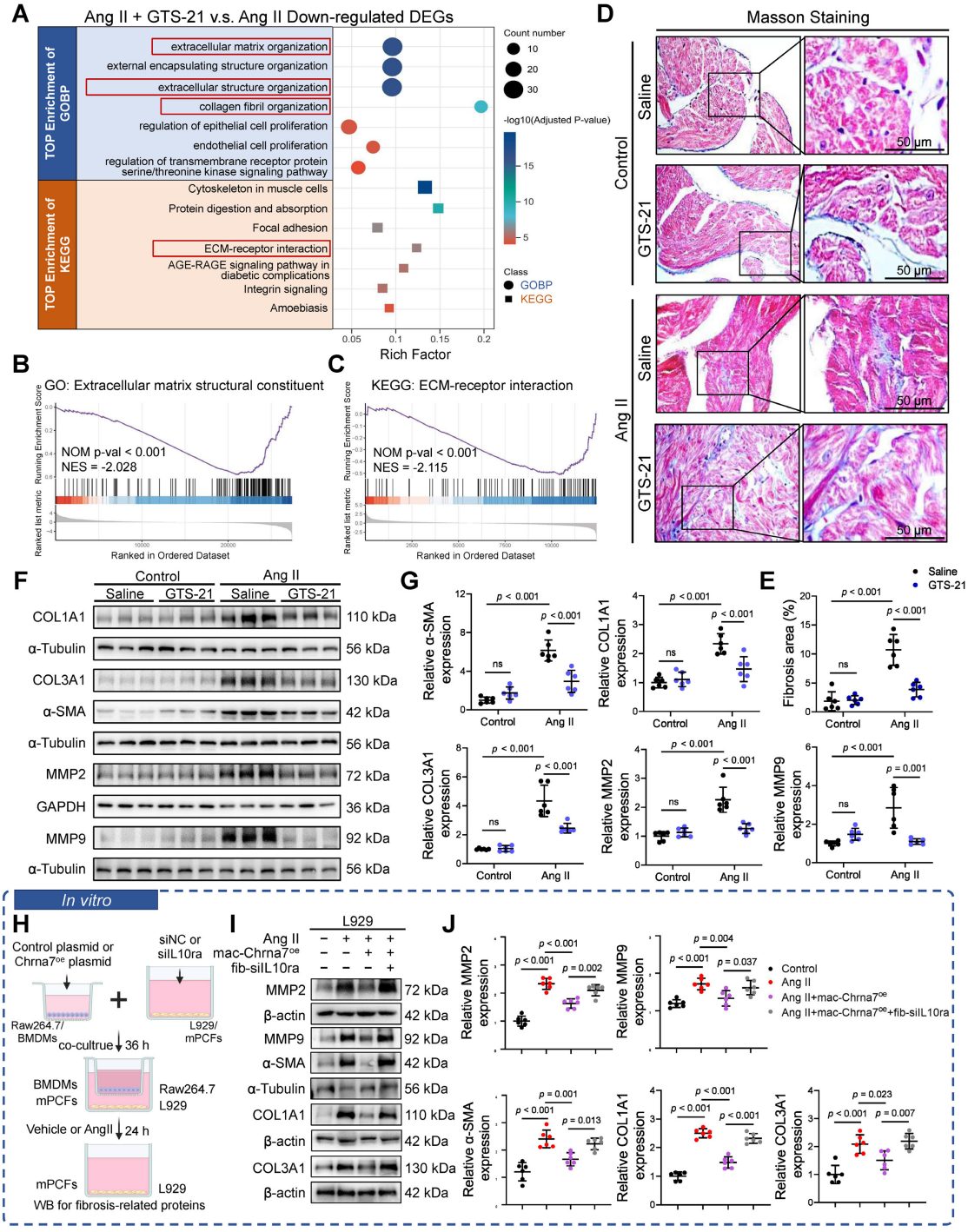


Figure 3. Inhibition of fibrotic signaling underlies the protective effect of macrophage α7nAChR activation on atrial remodeling mediated by IL-10. (A) Top down-regulated DEGs enrichment of GO analysis between Ang II + GTS-21 and Ang II group. (B) GSEA of extracellular matrix structural constituent signaling of GO. (C) GSEA of ECM-receptor interaction signaling of KEGG. (D-E) Representative micrographs of Masson trichrome staining and quantification of atrial fibrosis in mice receiving Saline or GTS-21 with/without Ang II infusion (n = 6; bar = 50 μm). (F-G) Western blotting and quantification of relative COL1A1, COL3A1, α-SMA, MMP2, and MMP9 expression in mice treated with GTS-21 or Saline with/without Ang II infusion (n = 6). The COL3A1 and α-SMA loading control reused that in Figure S1E (IL-1β); both are from the same blot. (H) Schematic diagram illustrating the process of Transwell co-culture systems. (I-J) Western blot analysis and quantification of MMP2, MMP9, COL1A1, COL3A1 and α-SMA in siIL10ra or NC infected L929 cells in the bottom compartment of the Transwell co-culture system with Raw264.7 macrophage Chrna7^{oe} and Ang II treatment. The COL1A1 loading control reused that in Figure 5I (ANKRD1); both are from the same blot. For statistics: two-way (E,G) or one-way (J) ANOVA with Tukey's post hoc test was applied; error bars denote S.D.; $p < 0.05$ was considered significant; ns, not significant.

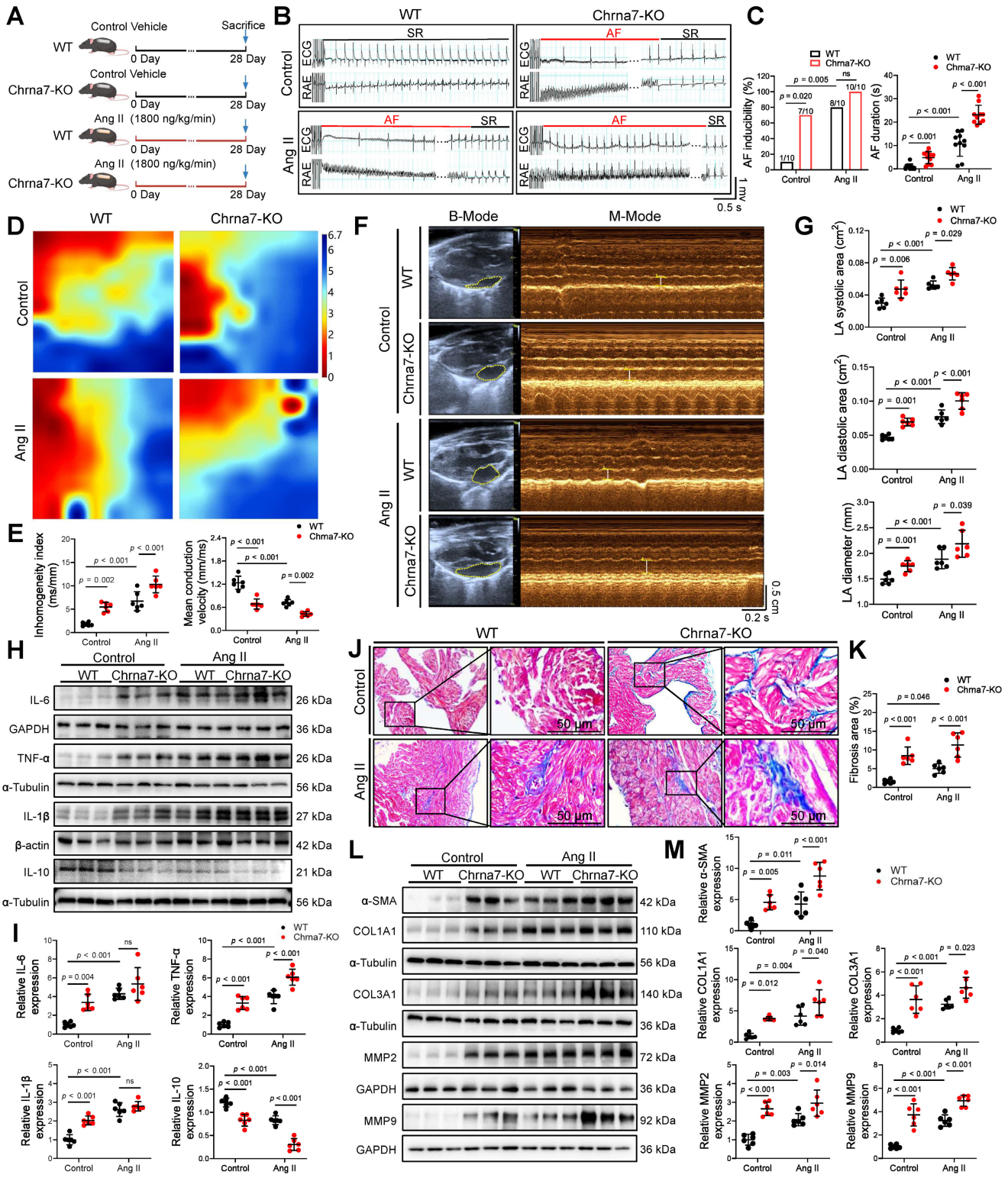


Figure 4. Loss of α7nAChR exacerbates Ang II-induced atrial remodeling in Chrna7-KO mice. (A) Chrna7-KO mice were predisposed to Ang II-induced AF. (B) Representative electrograms from surface ECG and RAE obtained during and after atrial pacing. (C) Quantified were both AF inducibility and AF duration (n = 10). (D-E) Representative electrophysiological maps of left atria are shown, along with quantification of inhomogeneity index and mean conduction velocity (n = 6). (F-G) Representative echocardiographic positioning, M-mode images, and quantification of LAAs, LAAd, LAD (n = 6). (H-I) Western blot analysis and quantification of relative IL-6, TNF-α, IL-1β and IL-10 protein expression in WT or Chrna7-KO mice with/without Ang II administration (n = 6). (J-K) Representative images of Masson trichrome staining and fibrotic quantification from the atria of WT and Chrna7-KO mice with/without Ang II infusion (n = 6; bar = 50 μm). (L-M) Immunoblot analysis and quantification of α-SMA, COL1A1, COL3A1, MMP2 and MMP9 in WT and Chrna7-KO mice with/without Ang II infusion (n = 6). Multiple comparisons were performed using two-way ANOVA with Tukey's post hoc test; error bars represent S.D.; AF inducibility was evaluated using Fisher's exact test; $p < 0.05$ was considered significant; ns indicates not significant.

ANKRD1 emerges as a key node in the α7nAChR-dependent macrophage to fibroblast axis

To identify potential mediators linking macrophage α7nAChR signaling to atrial fibrosis, we compared DEGs across three groups: Ang II versus Control, Ang II + GTS-21 versus Ang II, and Ang II + Chrna7-KO versus Ang II (Figure 5A). An UpSet plot analysis identified six shared DEGs (*Ankrd1*, *Tnfrsf12a*, *Hbegf*, *Kcnj6*, *Uts2b* and *Syndig1*) at the intersection of genes upregulated in Ang II versus Control, downregulated in Ang II + GTS-21 versus Ang II, and upregulated in Ang II + Chrna7-KO versus Ang II, among which *Ankrd1*, *Tnfrsf12a*, and *Hbegf* were closely associated with fibrosis (Figure 5B). Furthermore, correlation analysis of the three fibrosis-related DEGs whose expression was correlated with that of *Acta2*, a marker of fibroblast activation, using atrial appendage and fibroblast data from the GTEx database revealed that *Ankrd1* was most strongly positively correlated with *Acta2* ($R = 0.68$, $P < 0.0001$), highlighting ANKRD1 as a key candidate mediator (Figure S8A-C). Western blot analysis confirmed that Ang II markedly upregulated ANKRD1 protein expression, which was reversed by GTS-21 (Figure 5C-D), but increased in Chrna7-KO mice (Figure 5E-F). Co-immunofluorescence staining revealed that ANKRD1 expression was specifically increased in α-SMA-positive fibroblasts in the atria of Ang II mice; this enhancement was reduced by GTS-21 but increased in Chrna7-KO mice (Figure 5G, Figure S8D-F), suggesting that fibroblast-specific ANKRD1 serves as a key node mediated by macrophage α7nAChR activity.

To ascertain the effects of ANKRD1 on fibroblast activation and fibrosis, we treated Ang II in L929 cells and mPCFs with siANKRD1 (Figure S9A-C). *In vitro*, Ang II treatment of L929 fibroblasts or mPCFs upregulated ANKRD1 and fibrosis markers (α-SMA, MMP2, MMP9, COL1A1, and COL3A1), while ANKRD1 knockdown effectively abolished these effects (Figure S9D-G). Having previously demonstrated that IL-10 mediates α7nAChR-dependent macrophage-fibroblast communication, we herein further explored the potential link between IL-10 signaling and ANKRD1 in regulation of Ang II-induced fibrosis. Using the macrophage-fibroblast Transwell co-culture system (Figure 5H), we found that the overexpression of α7nAChR in Raw 264.7 macrophages or BMDMs (mac-Chrna7^{oe}) significantly attenuated the Ang II-induced upregulation of ANKRD1 in L929 fibroblasts and mPCFs, which was abrogated by the knockdown of the IL-10 receptor in fibroblasts (fib-siIL10ra) (Figure 5I-J, Figure S9H-I). Furthermore, the ELISA results showed that Ang II decreased the IL-10 level in the co-culture medium, which was restored by mac-Chrna7^{oe}, whereas fib-siIL10ra did not affect the secretion of IL-10 (Figure 5K, Figure S9J). Our findings suggest that IL-10 acts as a key mediator linking macrophage α7nAChR to fibroblast ANKRD1. To investigate the role of IL-10-mediated ANKRD1 regulation in fibrosis, we treated Ang II-stimulated L929 cells and mPCFs with recombinant IL-10 protein and an ANKRD1 overexpression (ANKRD1^{oe}) plasmid (Figure 5L). We found that IL-10 significantly suppressed the Ang II-treated upregulation of ANKRD1 and fibrotic markers, including α-SMA, MMP2, MMP9, COL1A1, and COL3A1. Notably, this anti-fibrotic effect was abolished by the ANKRD1^{oe} plasmid, suggesting that IL-10 mitigates fibrosis by downregulating ANKRD1 expression in L929 cells and mPCFs (Figure 5M-N, Figure S9K-L). Collectively, these findings identify ANKRD1 as a downstream effector of macrophage α7nAChR/IL-10 signaling and a key regulator of fibroblast activation, indicating that ANKRD1 acts as a molecular bridge in α7nAChR-dependent macrophage-fibroblast communication during atrial remodeling.

Macrophage α7nAChR attenuates fibrotic signaling by suppressing ANKRD1 nuclear translocation and AP-1/MMP9 binding in fibroblasts

To determine how macrophage α7nAChR influences fibroblast function, we employed a Transwell co-culture system comprising Raw264.7 macrophages or BMDMs transfected with Chrna7-overexpressing (mac-Chrna7^{oe}) cells cultivated in the upper chambers and L929 fibroblasts or mPCFs transfected with Flag-ANKRD1 (fib-ANKRD1^{oe}) cultivated in the lower chambers (Figure 6A). qPCR revealed that mac-Chrna7^{oe} suppressed Ang II-induced increases in the mRNA levels of *Ankrd1* and fibrotic markers (*Acta2*, *Col1a1*, *Col3a1*, *Mmp2*, and *Mmp9*) in L929 fibroblasts and mPCFs, and these effects were reversed by fib-ANKRD1^{oe}, particularly for MMP9 (Figure 6B, Figure S10A). Considering that ANKRD1 serves as a transcriptional regulator [37], we assessed the location of ANKRD1 in L929 fibroblasts and mPCFs in each group. Immunofluorescence analysis revealed that Ang II promoted ANKRD1 translocation from the cytoplasm to the nucleus in fibroblasts. Co-culture with Chrna7-overexpressing macrophages prevented Ang II-induced nuclear localization of ANKRD1 in L929 fibroblasts and mPCFs, and this effect was counteracted by fib-ANKRD1^{oe} (Figure 6C-D, Figure S10B-C). It has been shown that ANKRD1 protein was associated

with AP-1 family promoting effector genes of cancer-associated fibroblasts [25]. Our co-IP assay data revealed that ANKRD1 physically interacts with AP-1 components c-Fos and c-Jun in fibroblasts using co-IP assays (Figure 6E). This interaction was enhanced by Ang II and suppressed by Chrna7 overexpression in macrophages (Figure 6F). JASPAR prediction and ChIP assays revealed that Ang II upregulated AP-1 (c-Jun/c-Fos) binding to the *Mmp9* promoter, whereas co-culture with Chrna7-overexpressing macrophages reduced this binding. The overexpression of ANKRD1 in fibroblasts abrogated this reduction (Figure 6G). Together, these findings demonstrate that macrophage α7nAChR inhibits fibroblast ANKRD1 nuclear translocation and its cooperation with AP-1 at the MMP9 promoter, thus attenuating fibrotic activation.

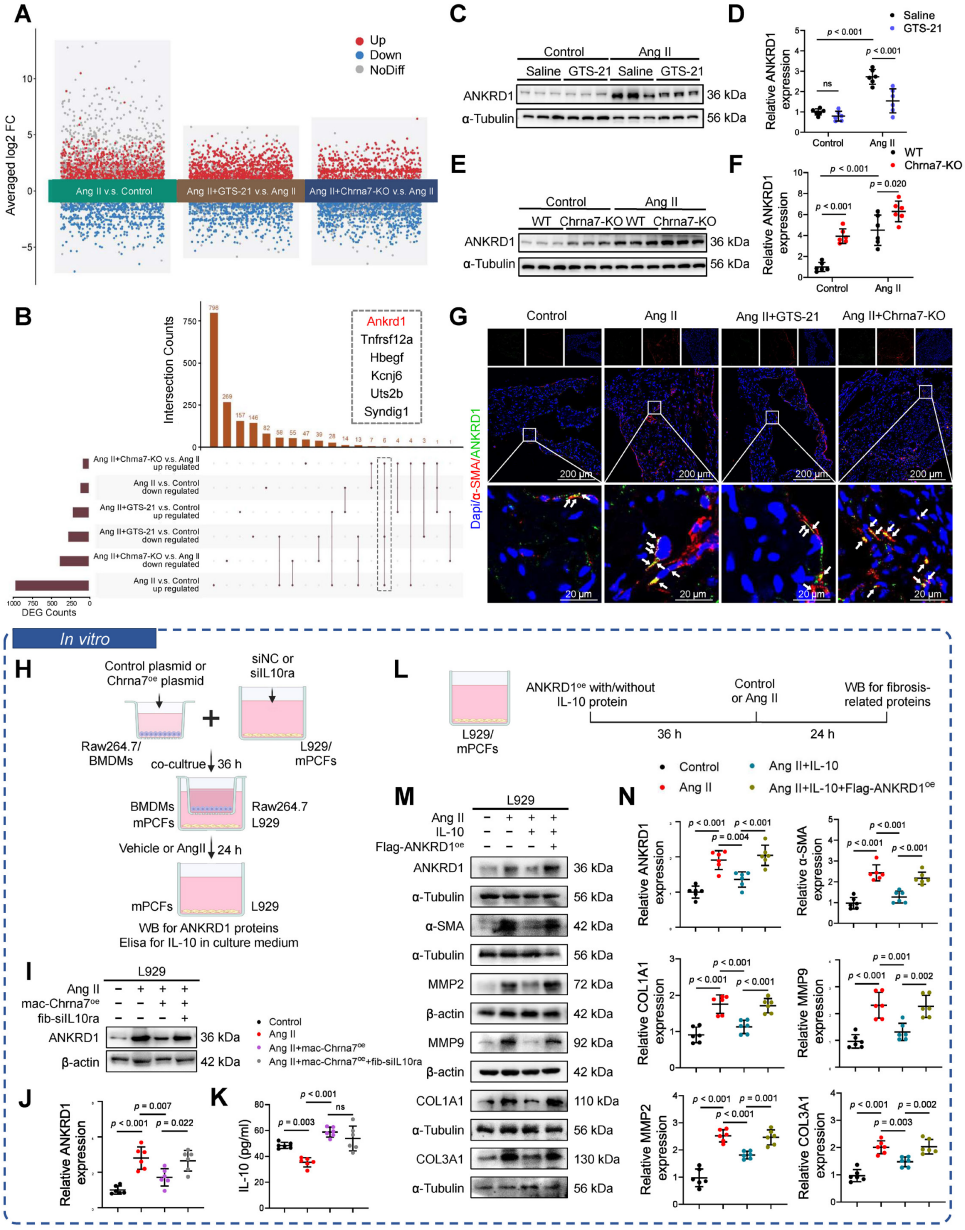


Figure 5. ANKRD1 emerges as a key node in α7nAChR-dependent macrophage to fibroblast axis. (A) Volcano plots showing DEGs in Ang II versus Control, Ang II + GTS-21 versus Ang II and Ang II + Chrna7-KO versus Ang II. (B) UpSet diagram depicting commonly up- or down-regulated DEGs among Ang II versus Control, Ang II + GTS-21 versus Ang II and Ang II + Chrna7-KO versus Ang II. (C-D) Immunoblot analysis and quantification of ANKRD1 in mice treated with GTS-21 or Saline with/without Ang II infusion (n = 6). (E-F) Immunoblot analysis and quantification of ANKRD1 in WT and Chrna7-KO mice with/without Ang II administration (n = 6). (G) Immunofluorescence images showing Dapi (blue), α-SMA (red) and ANKRD1 (green) in WT, Ang II-administered, Ang II + GTS-21-administered and Ang II + Chrna7-KO mice. White arrows mark the co-location of α-SMA and ANKRD1 (bar = 100 μm). (H) Schematic diagram illustrating the process of Transwell co-culture systems. (I-J) Representative immunoblots and quantification of ANKRD1 in siIL10ra or NC infected L929 cells in the Transwell bottom chamber of the co-culture system with Raw264.7 Chrna7^{oe} and Ang II treatment (n = 6). The ANKRD1 loading control reused that in Figure 3I (COL1A1); both are from the same blot. (K) Quantitative analysis of IL-10 in culture medium (n = 6). (L) Schematic diagram illustrating the treatment of ANKRD1 overexpression, IL-10 recombinant protein and Ang II in L929 cells or mPCFs. (M-N) Representative immunoblots and quantification of ANKRD1, α-SMA, MMP2, MMP9, COL1A1 and COL3A1 in L929 fibroblasts treated with Ang II and ANKRD1 overexpression with/without IL-10 protein (n = 6). Two-way (D,F) or one-way (J,K,N) ANOVA with Tukey's post hoc test was applied; error bars represent S.D. Significance: $p < 0.05$; ns, not significant.

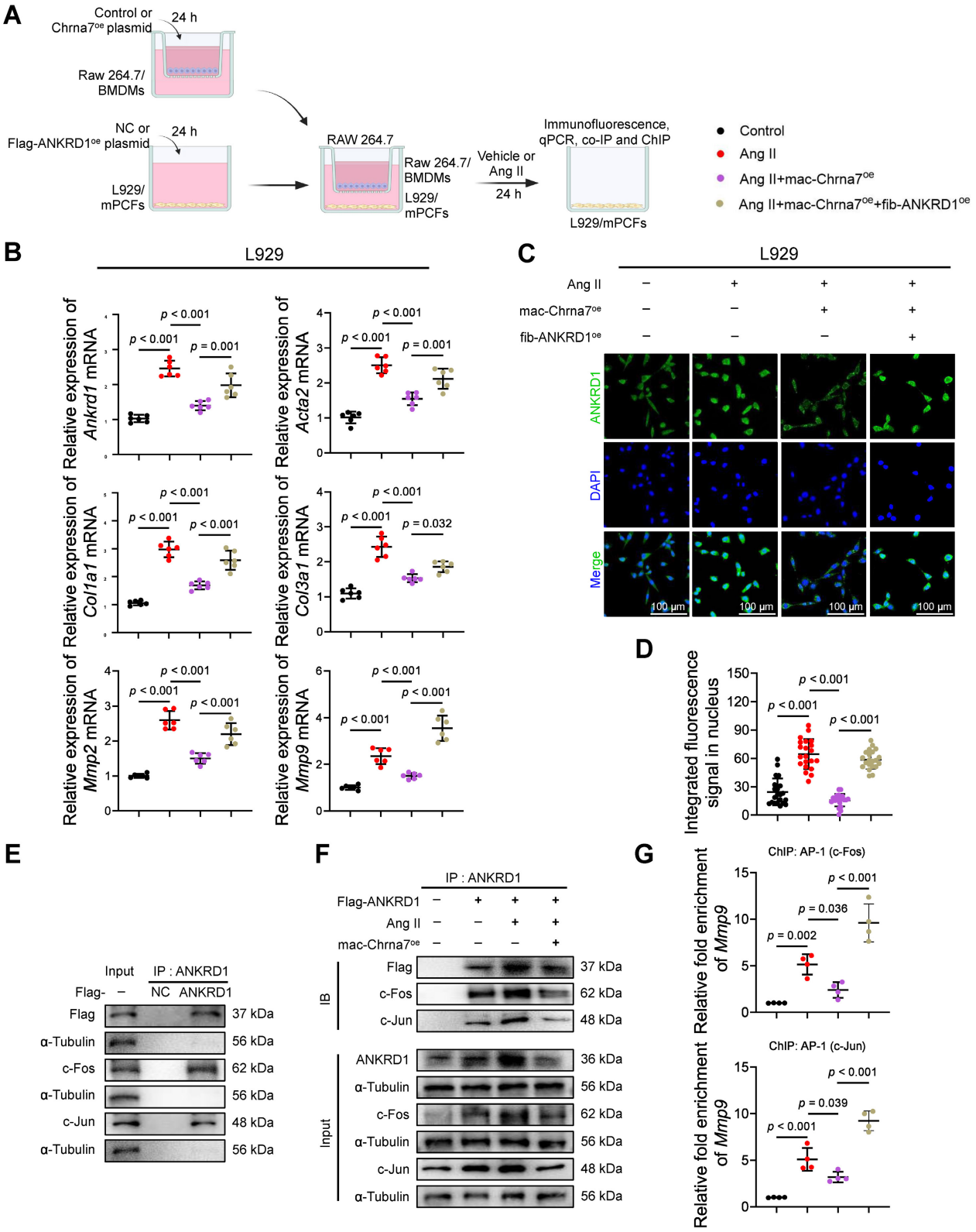


Figure 6. Macrophage α7nAChR attenuates fibrotic signaling by suppressing ANKRD1 nuclear translocation and AP-1/MMP9 binding in fibroblasts. (A) Schematic diagram illustrating the process of Transwell co-culture systems. (B) Quantitative analysis of *Ankrd1*, *Acta2*, *Col1a1*, *Col3a1*, *Mmp2* and *Mmp9* mRNA levels of L929 cells in the Transwell bottom chamber of the co-culture system with/without Raw264.7 Chrna7^{oe}, fibroblast Flag-ANKRD1^{oe} or Ang II incubation (n = 6). (C) Immunofluorescence imaging and quantification of ANKRD1 (green) and DAPI (blue) in L929 cells within the bottom compartment of the Transwell co-culture system (n = 21; scale bar = 100 μm). (D) Quantitation of integrated fluorescence signal in L929 fibroblasts nuclei. (E) Immunoblot analysis of Flag, c-Fos and c-Jun in Flag tagged ANKRD1 (Flag-ANKRD1) or empty vector-control (NC) infected L929 cells. (F) Immunoblot analysis of Flag, ANKRD1, c-Fos and c-Jun in Flag-ANKRD1 or NC infected L929 cells in the Transwell bottom chamber of the co-culture system with macrophage Chrna7^{oe} and Ang II treatment. (G) ChIP analysis of *Mmp9* promoter with anti-c-Fos and anti-c-Jun antibody in Flag-ANKRD1 or NC infected L929 cells in the Transwell bottom chamber of the co-culture system with macrophage Chrna7^{oe} and Ang II treatment (n = 4). Statistics: one-way ANOVA with Tukey's post hoc test; error bars, S.D.; $p < 0.05$ was considered significant; ns, not significant.

In vivo, fibroblast ANKRD1 overexpression abolishes the protective effects of macrophage-specific α7nAChR upregulation on Ang II-induced atrial remodeling

To validate the macrophage α7nAChR-fibroblast ANKRD1 axis *in vivo*, we used AAV-F4/80-Chrna7^{oe} to enhance macrophage α7nAChR expression and AAV-TCF21-ANKRD1^{oe} to overexpress ANKRD1 in fibroblasts in Ang II-infused mice (Figure S11A-D). Transvenous burst pacing revealed that Ang II + AAV-F4/80-Chrna7^{oe} mice (3/10) exhibited decreased AF inducibility and duration compared with the Ang II alone group (9/10). In contrast, Ang II + AAV-TCF21-ANKRD1^{oe} mice showed a marked increase (10/10). Furthermore, AAV-TCF21-ANKRD1^{oe} attenuated the protective effect of AAV-F4/80-Chrna7^{oe} against AF susceptibility (Figure 7A-C). Echocardiographic analyses revealed that while AAV-F4/80-Chrna7^{oe} treatment attenuated Ang II-induced enlargement of LAAd, LAAs, and LAD, which were counteracted by AAV-TCF21-ANKRD1^{oe}, which led to further dilation of the atrium (Figure 7D-G). Electrophysiological mapping further demonstrated that the restoration of conduction homogeneity by AAV-F4/80-Chrna7^{oe} was abrogated by AAV-TCF21-ANKRD1^{oe} in Ang II-treated mice (Figure 7H-J). Histological and Western blot analyses shown the anti-fibrosis effects of AAV-F4/80-Chrna7^{oe} in Ang II-treated mice, characterized by decreased Masson-positive staining (Figure 7K-L), reduced expression of fibrotic markers (MMP2, MMP9, α-SMA, COL1A1, COL3A1) (Figure 7M, S11E-I), downregulated pro-inflammatory cytokines (TNF-α, IL-6, and IL-1β) and upregulated anti-inflammatory cytokines (IL-10), all of which were counteracted by AAV-TCF21-ANKRD1^{oe} (Figure 7N, S11J-M). In summary, these findings establish that macrophage α7nAChR confers protection against Ang II-treated atrial remodeling and fibrosis by modulating fibroblast ANKRD1 expression.

Discussion

Our study demonstrated that macrophage α7nAChR activation protects against Ang II-induced atrial fibrillation through a macrophage-fibroblast signaling axis. Specifically, pharmacological activation or overexpression of macrophage α7nAChR corrects the balance of IL-10 related M1/M2c macrophage polarization. Subsequently, macrophage α7nAChR activity suppresses ANKRD1 nuclear translocation in fibroblasts, ultimately attenuating atrial inflammation and fibrosis. Importantly, we found that ANKRD1 nuclear translocation promotes fibrosis through the formation of a transcriptional complex with AP-1 and MMP9 to enhance enrichment in extracellular matrix structural composition, collagen fibril organization, and extracellular matrix-receptor interactions, effects that are mediated by macrophage α7nAChR. These findings provide new insights into the molecular mechanisms of atrial remodeling in AF driven by hypertensive and inflammatory pathologies.

AF is associated with significant cardiovascular morbidity and mortality [38]. Previous studies have demonstrated that low-level vagus nerve stimulation attenuates AF in humans and canines through activation of the α7nAChR-mediated cholinergic anti-inflammatory pathway [39, 40]. Our findings indicate that the activation of α7nAChR with GTS-21 effectively counteracted Ang II-induced prolongation of AF duration, enhanced AF susceptibility, atrial enlargement, and electrophysiological abnormalities in mice, primarily through suppression of inflammatory infiltration. Consistently, a previous investigation revealed that GTS-21 reduced sepsis-evoked AF in mice, further highlighting the critical role of α7nAChR in anti-inflammatory regulation [41]. To further confirm these observations, studies in Chrna7 knockout mice revealed that loss of α7nAChR aggravated Ang II-induced atrial dysfunction and structural remodeling, accompanied by increased expression of pro-inflammatory cytokines. A previous study has demonstrated that Chrna7 knockout exacerbates inflammatory responses, leading to functional deterioration after vascular injury [42]. Taken together with my findings, these studies suggest that α7nAChR may be a key factor in interrupting the link between inflammation and atrial fibrillation.

Macrophage α7nAChR functions as the key effector receptor that mediates the cholinergic anti-inflammatory pathway (CAP) [43]. A previous work has demonstrated that the activation of α7nAChR reduces inflammation, cardiac fibrosis, and cardiac hypertrophy mediated by the polarization of macrophages into anti-inflammatory subtypes [44]. Through co-localization experiments, we observed that GTS-21 and Chrna7 knockout strongly affected α7nAChR in macrophages, further confirming the role of α7nAChR in modulating macrophage function via the cholinergic anti-inflammatory pathway. Notably, previous studies have shown that the polarization of M2 macrophages toward the M2c phenotype facilitates rapid inflammation resolution and prevents the progression from renal injury to fibrosis [18]. *In vivo* and *in vitro* experiments have shown that Ang II promoted M1 macrophage polarization and suppressed M2/M2c macrophage polarization, which was mediated by IL-10.

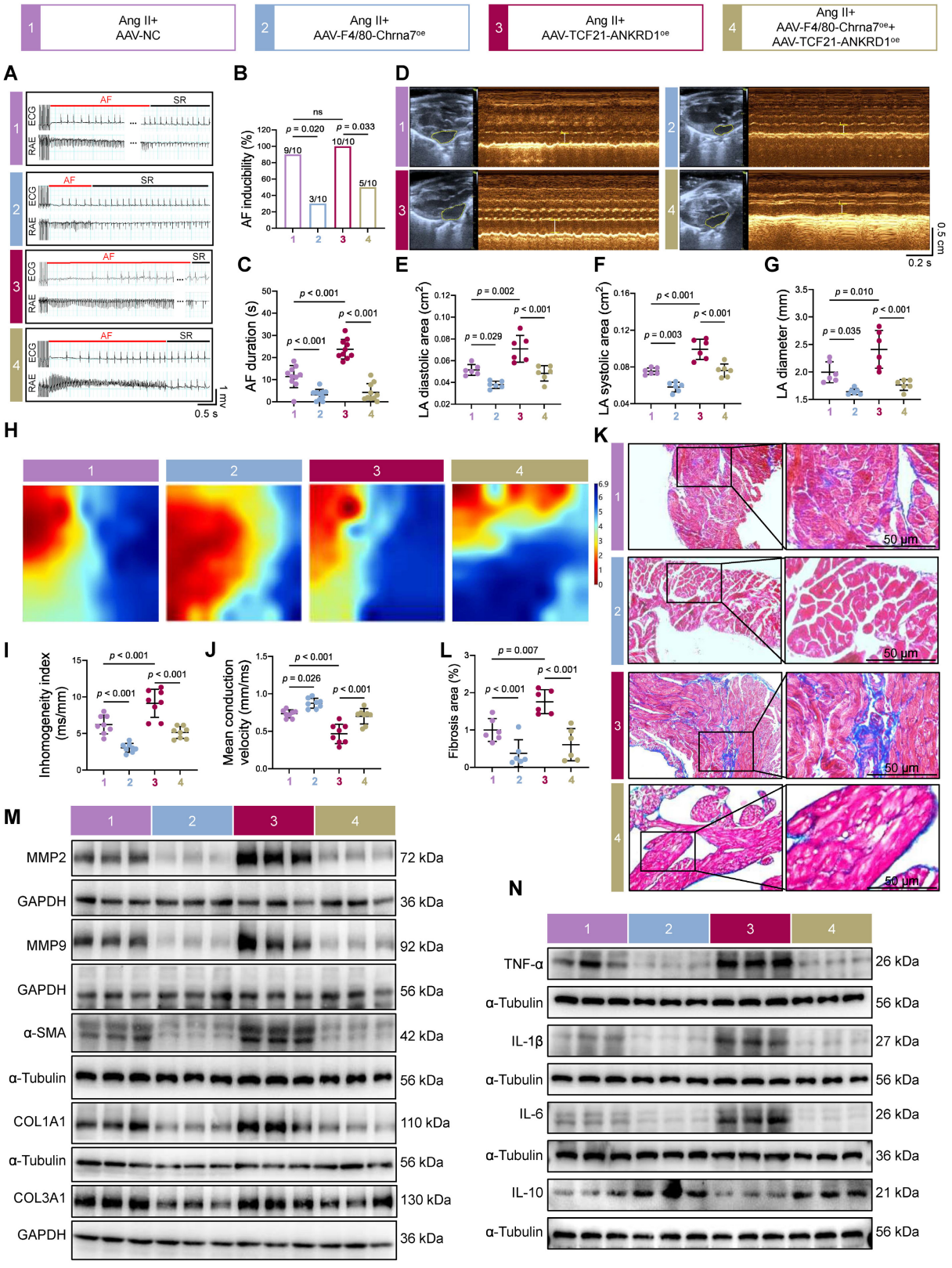


Figure 7. ***In vivo,*** **fibroblast ANKRD1 overexpression abolishes the protective effects of macrophage-specific α7nAChR upregulation on Ang II-induced atrial remodeling.** (A-C) Representative ECG and RAE recordings, together with quantification of AF inducibility and duration (n = 10). (D-G) Representative echocardiographic positioning, M-mode images, and quantification of LAAs, LAAd and LAD (n = 6). (H) Representative left atrial electrophysiological mapping. (I-J) Quantitatively assessed were mean conduction velocity and inhomogeneity index (n = 8). (K-L) Representative Masson trichrome-stained sections and quantification of atrial fibrosis (n = 6; bar = 50 μm). (M) Representative Western blots of MMP2, MMP9, α-SMA, COL1A1 and COL3A1 protein expression in mice atria. (N) Representative Western blots of TNF-α, IL-1β, IL-6 and IL-10 protein expression in mice atria. The loading controls for α-SMA in Figure 7M and IL-1β in Figure 7N were reused; both are from the same blot. The TNF-α loading control reused that in Figure S11B (ANKRD1); both are from the same blot. One-way ANOVA with Tukey's post hoc test; error bars, S.D.; Fisher's exact test for AF inducibility; $p < 0.05$; ns, not significant.

Pharmacological activation or overexpression of α7nAChR reversed the imbalance in IL-10-related M1/M2c macrophage polarization, suggesting that macrophage α7nAChR has a protective effect on atrial remodeling through IL-10 signaling. However, studies have revealed that α7nAChR activation in fibroblasts promotes right ventricular fibrosis and pulmonary hypertension [45], whereas the cardiomyocyte-specific deletion of α7nAChR ameliorates AF susceptibility in aged APP/PS1 mice [30]. This highlights the dual, and sometimes opposing, roles of α7nAChR in different cell types and disease contexts, which partially explains the discrepancies observed in systemic α7nAChR modulation across different studies. To further avoid the effects of α7nAChR on other cell types *in vivo*, we employed an adeno-associated virus specifically targeting macrophages (AAV-F4/80-Chrna7^{oe}), which effectively reversed Ang II-induced AF susceptibility, atrial dilatation and conduction velocity dysfunction and remodeling. Therefore, we believe that macrophage α7nAChR activity can ameliorate atrial dysfunction and remodeling in hypertensive inflammatory AF.

Fibrosis, which is primarily mediated by fibroblasts, constitutes a major substrate for atrial remodeling in AF [46]. M1 macrophage polarization and the resulting inflammatory responses exacerbate cardiac fibroblast-mediated fibrosis, thus contributing to AF in rheumatoid arthritis rats [47]. We performed RNA-Seq of atrial tissues from Ang II-infused mice with or without GTS-21 treatment or Chrna7-KO to explore the signaling networks underlying α7nAChR-mediated atrial protection. Our data indicated that fibrosis-related signaling was among the most significantly enriched pathways and was associated with ANKRD1. Previous studies have shown that ANKRD1 is involved in fibrosis across multiple organs, including the heart, liver, kidneys, etc. [24, 48, 49]. Moreover, previous investigation revealed that ANKRD1 expression is increased upon Ang II stimulation, contributing to cardiac hypertrophy [50], whereas elevated ANKRD1 levels have detrimental effects on cardiac function by promoting fibrosis and aggravating cardiac remodeling [51]. We also confirmed the upregulation of ANKRD1 in Ang II-treated mice and L929 fibroblasts mediated by IL-10, and found that ANKRD1 knockdown effectively inhibited Ang II-induced fibrotic responses in fibroblasts. Consequently, we propose that macrophage α7nAChR may regulate fibrosis-associated atrial remodeling through the modulation of fibroblast ANKRD1. However, the precise IL-10 receptor downstream pathways responsible for ANKRD1 remain unknown and warrant further investigation using inhibitor-based or genetic approaches.

Atrial fibroblasts and macrophages have long been recognized as key participants in hypertension-driven inflammatory AF, with increasing evidence suggesting functional crosstalk between them [52, 53]. A previous study demonstrated that macrophages influence fibroblasts through the release of M1 polarization-associated factors in Ang II-treated AF [54]. In our work, the results of the Transwell co-culture system indicated that upregulation of macrophage α7nAChR expression alleviated Ang II-treated inflammatory cytokine production and reduced the protein expression of pro-fibrotic markers, including ANKRD1, in fibroblasts. ANKRD1 exhibits dual subcellular localization, and its translocation to the nucleus facilitates positive transcriptional regulation, likely through its function as a transcriptional cofactor rather than a direct transcription factor [55]. Recent investigations have revealed that ANKRD1 interacts with AP-1 family members and binds to promoter or enhancer regions of fibroblast effector genes, such as *Mmp9*, thereby promoting the activation of cancer-associated fibroblasts [24, 56]. Similarly, our data confirmed the interaction between ANKRD1 and c-Fos/c-Jun in L929 cells, enhanced in response to Ang II treatment, but was inhibited by macrophage α7nAChR overexpression. Additionally, overexpression of macrophage α7nAChR reversed the Ang II-elicited transcriptional activation of MMP9 by c-Fos and c-Jun, which was, however, counteracted by ANKRD1 upregulation in L929 fibroblasts. Our data indicated that macrophage α7nAChR attenuated fibrotic activation via inhibiting fibroblast ANKRD1 nuclear translocation and cooperation with AP-1 at the MMP9 promoter. Finally, *in vivo*, we demonstrated that fibroblast-specific overexpression of ANKRD1 attenuated the protective effects of macrophage-specific α7nAChR upregulation against Ang II-induced atrial remodeling and fibrosis. These novel findings underscore the α7nAChR-dependent role of macrophage-to-fibroblast communication in atrial fibrosis, providing a potential therapeutic target in the development of hypertensive inflammatory AF.

Nevertheless, several limitations of our study should be mentioned. First, our conclusions are primarily derived from the Ang II infusion model, which specifically recapitulates hypertension-associated inflammatory atrial remodeling. However, atrial fibrillation is a heterogeneous disease. Our current study design did not account for other distinct pathological substrates, such as aging-related degeneration or mechanical stretch-induced remodeling. Consequently, the applicability of the α7nAChR-ANKRD1 axis to multi-substrates of the AF

model, such as HOMER (which combines hypertension, obesity, and mitral valve regurgitation) [57], remains to be determined. Second, the potential interactions of ANKRD1 with other transcription factors warrant further investigation using Co-IP coupled with mass spectrometry (Co-IP-MS) and Co-IP sequencing (Co-IP-seq). Third, although we utilized primary cardiac fibroblasts to increase their physiological relevance, we acknowledge that compared with atrial-specific fibroblasts, general cardiac fibroblasts may exhibit spatial and functional heterogeneity. Future studies should employ atrial-specific isolation to further validate these findings. Finally, although we provide a mechanistic integration, the translational implications are currently based on mouse data. Future research involving human clinical specimens is essential to confirm the relevance of the α7nAChR-ANKRD1 axis in human atrial fibrillation.

Conclusion

Our study elucidates a key mechanistic integration wherein macrophage α7nAChR signaling mitigates hypertensive inflammatory atrial remodeling. Specifically, we demonstrate that this pathway attenuates fibrosis by modulating ANKRD1-mediated AP-1/MMP9 activity in fibroblasts. These findings provide a theoretical basis for exploring α7nAChR-targeted strategies for treating atrial fibrillation driven by hypertensive and inflammatory pathologies.

Abbreviations

α7nAChR: alpha7 nicotinic acetylcholine receptor; α-SMA: alpha-smooth muscle actin; AAV: adeno-associated virus; AF: atrial fibrillation; Ang II: angiotensin II; ANKRD1: ankyrin repeat domain 1; AP-1: activator protein-1; APC: allophycocyanin; Arg1: arginase 1; BMDM: bone marrow-derived macrophage; CAP: cholinergic anti-inflammatory pathway; CCK-8: Cell Counting Kit-8; ChIP: chromatin immunoprecipitation; Chrna7: cholinergic receptor nicotinic alpha 7 subunit; Co-IP: co-immunoprecipitation; COL1A1: collagen type I alpha 1; COL3A1: collagen type III alpha 1; Cy7: cyanine dye 7; DEGs: differentially expressed genes; ECM: extracellular matrix; GAPDH: glyceraldehyde-3-phosphate dehydrogenase; GO: Gene Ontology; GSEA: Gene Set Enrichment Analysis; GTEx: Genotype-Tissue Expression; GTS-21: selective α7nAChR agonist; IL-1β: interleukin-1 beta; IL-6: interleukin-6; IL-10: interleukin-10; iNOS: inducible nitric oxide synthase; KEGG: Kyoto Encyclopedia of Genes and Genomes; LAD: left atrial diameter; LAAd: left atrial diastolic area; LAAs: left atrial systolic area; LVEF: left ventricular ejection fraction; M-CSF: macrophage colony-stimulating factor; MMP2: matrix metalloproteinase 2; MMP9: matrix metalloproteinase 9; qPCR: quantitative real-time PCR; RNA-seq: RNA sequencing; TCF21: transcription factor 21; TNF-α: tumor necrosis factor-alpha; WT: wild-type.

Supplementary Material

Supplementary figures and table.
https://www.thno.org/v17p0468s1.pdf

Acknowledgements

This study is supported by the funds from the National Natural Science Foundation of China (82300356, 82570388), Central Government-guided Local Science and Technology Development Fund-Youth Category B (2026JH6/101000001), Shenyang Science and Technology Project (24-214-3-149), Independent scientific research project of General Hospital of Northern Theater Command (ZZKY2024069).

Authorship contributions

Ling Dong, Jikai Zhao, Jinsong Han, Huishan Wang conceptualized the study and conducted the experiments. Ling Dong, Yiwen Wang, Zhenduo Zhang, Ting Yan, Liman Yang, Tao Huang, Liming Yu provided technical assistance during the experiments. Ling Dong, Tong Su, Yinli Xu, Boxuan Sun, Zijun Zhou, Jiyuan Zhan performed experimental data collection and analysis. Ling Dong, Jikai Zhao, Jinsong Han, Huishan Wang drafted the article and critically revised the manuscript.

Data availability statement

The data underlying this article will be shared on reasonable request to the corresponding author.

Competing Interests

The authors have declared that no competing interest exists.

References

1. Yamamoto C, Trayanova NA. Atrial fibrillation: Insights from animal models, computational modeling, and clinical studies. EBioMedicine. 2022; 85: 104310
2. Morin DP, Bernard ML, Madias C, Rogers PA, Thihalolipavan S, Estes NAM. The State of the art: atrial fibrillation epidemiology, prevention, and treatment. Mayo Clin Proc. 2016; 91: 1778-810
3. Zimetbaum P. Atrial fibrillation. Ann Intern Med. 2017; 166: ITC33-ITC48
4. Chen X, Yu L, Meng S, Zhao J, Huang X, Wang Z, et al. Inhibition of TREM-1 ameliorates angiotensin II-induced atrial fibrillation by attenuating macrophage infiltration and inflammation through the PI3K/AKT/FoxO3a signaling pathway. Cell signal. 2024; 124: 111458
5. Zhao J, Zhang Y, Yin Z, Zhu Y, Xin F, Zhang H, et al. Impact of proinflammatory epicardial adipose tissue and differentially enhanced autonomic remodeling on human atrial fibrillation. J Thorac Cardiovasc Surg. 2023; 165: e158-e74

6. Nattel S. Molecular and cellular mechanisms of atrial fibrosis in atrial fibrillation. JACC Clin Electrophysiol. 2017; 3: 425-35
7. Zhang Y, Yuan M, Cai W, Sun W, Shi X, Liu D, et al. Prostaglandin I2 signaling prevents angiotensin II-induced atrial remodeling and vulnerability to atrial fibrillation in mice. Cell Mol Life Sci. 2024; 81: 264
8. Hulsmans M, Sam F, Nahrendorf M. Monocyte and macrophage contributions to cardiac remodeling. J Mol Cell Cardiol. 2016; 93: 149-55
9. Gao Z, Yan L, Meng J, Lu Z, Ge K, Jiang Z, et al. Targeting cardiac fibrosis with chimeric antigen receptor macrophages. Cell Discov. 2024; 10: 86
10. Hulsmans M, Clauss S, Xiao L, Aguirre AD, King KR, Hanley A, et al. Macrophages facilitate electrical conduction in the heart. Cell. 2017; 169: 510-22. e20
11. Lee C, Jeong H, Lee H, Hong M, Park SY, Bae H. Magnolol attenuates cisplatin-induced muscle wasting by M2c macrophage activation. Front Immunol. 2020; 11: 77
12. Luo L, Wang S, Hu Y, Wang L, Jiang X, Zhang J, et al. Precisely regulating M2 subtype macrophages for renal fibrosis resolution. ACS Nano. 2023; 17: 22508-26
13. Noviello CM, Gharpure A, Mukhtasimova N, Cabuco R, Baxter L, Borek D, et al. Structure and gating mechanism of the α7 nicotinic acetylcholine receptor. Cell. 2021; 184: 2121-34. e13
14. Han X, Li W, Li P, Zheng Z, Lin B, Zhou B, et al. Stimulation of α7 nicotinic acetylcholine receptor by nicotine suppresses decidual M1 macrophage polarization against inflammation in lipopolysaccharide-induced preeclampsia-like mouse model. Front Immunol. 2021; 12: 642071
15. Burke SM, Avstrikova M, Noviello CM, Mukhtasimova N, Changeux J-P, Thakur GA, et al. Structural mechanisms of α7 nicotinic receptor allosteric modulation and activation. Cell. 2024; 187: 1160-76. e21
16. Li G, Zhang C, Li Y, Yang J, Wu J, Shao Y, et al. Optogenetic vagal nerve stimulation attenuates heart failure by limiting the generation of monocyte-derived inflammatory CCRL2$^+$ macrophages. Immunity. 2025; 58: 1847-61. e9
17. Lu J, Chen K, Cen Z, Huang Y, Li Y, Chen L, et al. α7nAChR on B cells directs T cell differentiation to prevent viral myocarditis. JCI Insight. 2025; 10: e189323
18. Hoover DB. Cholinergic modulation of the immune system presents new approaches for treating inflammation. Pharmacol Ther. 2017; 179: 1-16
19. Embregts CWE, Begeman L, Voesenek CJ, Martina BEE, Koopmans MPG, Kuiken T, et al. Street RABV induces the cholinergic anti-inflammatory pathway in human monocyte-derived macrophages by binding to nAChr α7. Front Immunol. 2021; 12: 622516
20. Chung CH, Bretherton B, Zainalabidin S, Deuchars SA, Deuchars J, Mahadi MK. Mediation of cardiac macrophage activity via auricular vagal nerve stimulation ameliorates cardiac ischemia/reperfusion injury. Front Neurosci. 2020; 14: 906
21. Ling S, Chen Y-T, Wang J, Richards A, Liew O. Ankyrin repeat domain 1 protein: a functionally pleiotropic protein with cardiac biomarker potential. Int J Mol Sci. 2017; 18: 1362
22. Miller MK, Bang M-L, Witt CC, Labeit D, Trombitas C, Watanabe K, et al. The muscle ankyrin repeat proteins: CARP, ankrd2/Arpp and DARP as a family of titin filament-based stress response molecules. J Mol Biol. 2003; 333: 951-64
23. Collins AR, Schnee J, Wang W, Kim S, Fishbein MC, Bruemmer D, et al. Osteopontin modulates angiotensin II- induced fibrosis in the intact murine heart. J Am Coll Cardiol. 2004; 43: 1698-705
24. Meng H, Du Z, Lu W, Wang Q, Sun X, Jiang Y, et al. Baoyuan decoction (BYD) attenuates cardiac hypertrophy through ANKRD1-ERK/GATA4 pathway in heart failure after acute myocardial infarction. Phytomedicine. 2021;89: 153617
25. Mazzeo L, Ghosh S, Di Cicco E, Isma J, Tavernari D, Samarkina A, et al. ANKRD1 is a mesenchymal-specific driver of cancer-associated fibroblast activation bridging androgen receptor loss to AP-1 activation. Nat Commun. 2024; 15: 1038
26. Bin L, Li X, Richers B, Streib JE, Hu JW, Taylor P, et al. Ankyrin repeat domain 1 regulates innate immune responses against herpes simplex virus 1: a potential role in eczema herpeticum. J Allergy Clin Immunol. 2018; 141: 2085-93. e1
27. Liu XH, Bauman WA, Cardozo C. ANKRD1 modulates inflammatory responses in C2C12 myoblasts through feedback inhibition of NF-κB signaling activity. Biochem Biophys Res Commun. 2015;464(1): 208-13
28. Xu B, Xu Y, Ren W, Meng S, Hong T, Cao Z, et al. S-Methyl-L-cysteine targeting MsrA attenuates Ang II-induced oxidative stress and atrial remodeling via the p38 MAPK signaling pathway. Food Funct. 2024; 15: 9165-75
29. Yu LM, Dong X, Huang T, Zhao JK, Zhou ZJ, Huang YT, et al. Inhibition of ferroptosis by icariin treatment attenuates excessive ethanol consumption-induced atrial remodeling and susceptibility to atrial fibrillation, role of SIRT1. Apoptosis. 2023; 28: 607-26
30. Zhao J, Yu L, Xue X, Xu Y, Huang T, Xu D, et al. Diminished α7 nicotinic acetylcholine receptor (α7nAChR) rescues amyloid-β induced atrial remodeling by oxi-CaMKII/MAPK/AP-1 axis-mediated mitochondrial oxidative stress. Redox Biol. 2023; 59: 102594
31. Zhao J, Xu Y, Gao Y, Yan T, Meng S, Hong T, et al. A novel lncRNA MSTRG.16386.1 as ceRNA promotes kidney injury induced by deep hypothermic circulatory arrest via mediating miR-466b-5p/Spry2 axis. FASEB J. 2026; 40: e71342
32. Chen C, Chen H, Zhang Y, Thomas HR, Frank MH, He Y, et al. TBtools: An Integrative Toolkit Developed for Interactive Analyses of Big Biological Data. Mol Plant. 2020;13(8): 1194-1202
33. Lex A, Gehlenborg N, Strobelt H, Vuillemot R, Pfister H. UpSet: Visualization of Intersecting Sets. IEEE Trans Vis Comput Graph. 2014;20(12): 1983-92
34. Miao YR, Xia M, Luo M, Luo T, Yang M, Guo AY. ImmuCellAI-mouse: a tool for comprehensive prediction of mouse immune cell abundance and immune microenvironment depiction. Bioinformatics. 2022; 38: 785-91
35. Jung M, Ma Y, Iyer RP, DeLeon-Pennell KY, Yabluchanskiy A, Garrett MR, et al. IL-10 improves cardiac remodeling after myocardial infarction by stimulating M2 macrophage polarization and fibroblast activation. Basic Res Cardiol. 2017; 112: 33
36. Liu EYL, Xia Y, Kong X, Guo MSS, Yu AXD, Zheng BZY, et al. Interacting with α7nAChR is a new mechanism for AChE to enhance the inflammatory response in macrophages. Acta Pharm Sin B. 2020; 10: 1926-42
37. Zhong L, Chiusa M, Cadar AG, Lin A, Samaras S, Davidson JM, et al. Targeted inhibition of ANKRD1 disrupts sarcomeric ERK-GATA4 signal transduction and abrogates phenylephrine-induced cardiomyocyte hypertrophy. Cardiovasc Res. 2015; 106: 261-271
38. Song W, Shangguan W, Lin W, Di C, Zhou J, Zhang F, et al. Efficacy and Safety of Left Atrial Substrate Modification by Cryoballoon Ablation in Persistent Atrial Fibrillation: Study Protocol for a Randomized Controlled Trial (LACA Trial). Heart Mind, 2026, 10(3), 161–168.
39. Stavrakis S, Humphrey MB, Scherlag BJ, Hu Y, Jackman WM, Nakagawa H, et al. Low-level transcutaneous electrical vagus nerve stimulation suppresses atrial fibrillation. J Am Coll Cardiol. 2015; 65: 867-75
40. Yu L, Dyer JW, Scherlag BJ, Stavrakis S, Sha Y, Sheng X, et al. The use of low-level electromagnetic fields to suppress atrial fibrillation. Heart Rhythm. 2015; 12: 809-17
41. Zhou J, Wu K, Ma Y, Zhu J, Zhou Y, Zhang Z, et al. GTS-21 alleviates sepsis-induced atrial fibrillation susceptibility by modulating macrophage polarization and Neuregulin-1 secretion. Int immunopharmacol. 2025; 154: 114561
42. Li DJ, Fu H, Tong J, Li YH, Qu LF, Wang P, et al. Cholinergic anti-inflammatory pathway inhibits neointimal hyperplasia by suppressing inflammation and oxidative stress. Redox Biol. 2018; 15: 22-33
43. Wang H, Yu M, Ochani M, Amella CA, Tanovic M, Susarla S, et al. Nicotinic acetylcholine receptor alpha7 subunit is an essential regulator of inflammation. Nature. 2003; 421: 384-388
44. Su Y, Zhang W, Zhang R, Yuan Q, Wu R, Liu X, et al. Activation of cholinergic anti-inflammatory pathway ameliorates cerebral and cardiac dysfunction after intracerebral hemorrhage through autophagy. Front Immunol. 2022; 13: 870174
45. Vang A, da Silva Gonçalves Bos D, Fernandez-Nicolas A, Zhang P, Morrison AR, Mancini TJ, et al. α7 Nicotinic acetylcholine receptor mediates right ventricular fibrosis and diastolic dysfunction in pulmonary hypertension. JCI Insight. 2021; 6: e142945
46. Sohns C, Marrouche NF. Atrial fibrillation and cardiac fibrosis. Eur Heart J. 2020; 41: 1123-31
47. Han X, Gao Y, He M, Luo Y, Wei Y, Duan Y, et al. Evolocumab prevents atrial fibrillation in rheumatoid arthritis rats through restraint of PCSK9 induced atrial remodeling. J Adv Res. 2024; 61: 211-21
48. Ghosh AK, Murphy SB, Kishore R, Vaughan DE. Global gene expression profiling in PAI-1 knockout murine heart and kidney: molecular basis of cardiac-selective fibrosis. PLoS One. 2013; 8: e63825
49. Mannaerts I, Leite SB, Verhulst S, Claerhout S, Eysackers N, Thoen LFR, et al. The Hippo pathway effector YAP controls mouse hepatic stellate cell activation. J Hepatol. 2015; 63: 679-88
50. Chen C, Shen L, Cao S, Li X, Xuan W, Zhang J, et al. Cytosolic CARP promotes angiotensin II- or pressure overload-induced cardiomyocyte hypertrophy through calcineurin accumulation. PLoS One. 2014; 9: e104040
51. Xu X, Wang X, Li Y, Chen R, Wen H, Wang Y, et al. Research progress of ankyrin repeat domain 1 protein: an updated review. Cell Mol Biol Lett. 2024; 29: 131
52. Yamashita T, Sekiguchi A, Iwasaki YK, Date T, Sagara K, Tanabe H, et al. Recruitment of immune cells across atrial endocardium in human atrial fibrillation. Circ J. 2010; 74: 262-70

53. Su R, Song L, Liu Y, Zhang C, Xie L, Han Z. Macrophage-fibroblast crosstalk in fibrosis: key regulator of fibrosis across different organs. Front Biosci (Landmark Ed). 2025; 30: 38864
54. Chen XQ, Zhang DL, Zhang MJ, Guo M, Zhan YY, Liu F, et al. TRIF promotes angiotensin II-induced cross-talk between fibroblasts and macrophages in atrial fibrosis. Biochem Biophys Res Commun. 2015; 464: 100-5
55. Xie R, Yuan S, Hu G, Zhan J, Jin K, Tang Y, et al. Nuclear AGO2 promotes myocardial remodeling by activating ANKRD1 transcription in failing hearts. Mol Ther. 2024; 32: 1578-94
56. Hu L, Zheng C, Kong Y, Luo Z, Huang F, Zhu Z, et al. Cathepsin G promotes arteriovenous fistula maturation by positively regulating the MMP2/MMP9 pathway. Ren Fail. 2024; 46: 2316269
57. Hulsmans M, Schloss MJ, Lee IH, Bapat A, Iwamoto Y, Vinegoni C, et al. Recruited macrophages elicit atrial fibrillation. Science. 2023; 381: 231-9